Monthly Notices
of the
ROYAL ASTRONOMICAL SOCIETY

MNRAS **474,** 3760–3781 (2018)
Advance Access publication 2017 November 25

doi:10.1093/mnras/stx3013

Widespread SiO and CH_3OH emission in filamentary infrared dark clouds

G. Cosentino,[1⋆] I. Jiménez-Serra,[2] J. D. Henshaw,[3] P. Caselli,[4] S. Viti,[1] A. T. Barnes,[3,4] F. Fontani,[5] J. C. Tan[6] and A. Pon[7]

[1]*Department of Physics and Astronomy, University College London, Gower Street, London WC1E 6BT, UK*
[2]*Astronomy Unit, Queen Mary University of London, Mile End Road, London E1 4NS, UK*
[3]*Max Planck Institute for Astronomy, Königstuhl 17, D-69117 Heidelberg, Germany*
[4]*Max Planck Institute for Extraterrestrial Physics, Giessenbachstrasse 1, D-85748 Garching bei München, Germany*
[5]*INAF – Osservatorio Astronomico di Arcetri, Largo E. Fermi 5, I-50125 Florence, Italy*
[6]*Departments of Astronomy and Physics, University of Florida, Gainesville, FL 32611, USA*
[7]*Department of Physics and Astronomy, The University of Western Ontario, 1151 Richmond Street, London, ON N6A 3K7, Canada*

Accepted 2017 November 16. Received 2017 November 16; in original form 2017 June 7

ABSTRACT

Infrared dark clouds (IRDCs) are cold, dense regions of high (optical and infrared) extinction, believed to be the birthplace of high-mass stars and stellar clusters. The physical mechanisms leading to the formation of these IRDCs are not completely understood and it is thus important to study their molecular gas kinematics and chemical content to search for any signature of the IRDCs formation process. Using the 30-m-diameter antenna at the Instituto de Radioastronomía Milimétrica (IRAM), we have obtained emission maps of dense gas tracers ($H^{13}CO^+$ and $HN^{13}C$) and typical shock tracers (SiO and CH_3OH) towards three IRDCs, G028.37+00.07, G034.43+00.24, and G034.77−00.55 (clouds C, F, and G, respectively). We have studied the molecular gas kinematics in these clouds and, consistent with previous works towards other IRDCs, the clouds show complex gas kinematics with several velocity-coherent substructures separated in velocity space by a few km s^{-1}. Correlated with these complex kinematic structures, widespread (parsec-scale) emission of SiO and CH_3OH is present in all the three clouds. For clouds C and F, known to be actively forming stars, widespread SiO and CH_3OH is likely associated with on-going star formation activity. However, for cloud G, which lacks either 8 or 24 μm sources and 4.5 μm H_2 shock-excited emission, the detected widespread SiO and CH_3OH emission may have originated in a large-scale shock interaction, although a scenario involving a population of low-mass stars driving molecular outflows cannot be fully ruled out.

Key words: stars: formation – ISM: individual objects: G028.37+00.07 – ISM: individual objects: G034.43+00.24 – ISM: individual objects: G034.77−00.55 – ISM: molecules.

1 INTRODUCTION

The process that leads to the formation of high-mass stars (stars with masses $>8\,M_\odot$) is still under debate. The difficulty in tracing their evolutionary path lies in their short evolutionary time-scales, their crowded cluster environments, and the large distances at which they are typically found. In addition, their strong feedback [stellar winds, supernovae explosions, and ultraviolet (UV) radiation] largely affects their birth place, making the study of their formation processes even more challenging.

One way to circumvent the problem of feedback is to study the earliest stages of high-mass star formation represented by infrared dark clouds (IRDCs; Rathborne, Jackson & Simon 2006; Simon et al. 2006; Peretto & Fuller 2010; Butler & Tan 2012). IRDCs are cold ($T \leq 25$ K; Pillai et al. 2006), dense ($n(H_2) \geq 10^5$ cm^{-3}), and highly extinguished ($A_v \geq 100$ mag and $N(H_2) \geq 10^{22}$ cm^{-2}; Butler & Tan 2009, 2012) molecular clouds, first observed in extinction against the bright mid-infrared (IR) Galactic background (Perault et al. 1996; Egan et al. 1998). The morphology ranges globular to very filamentary, with the latter morphology likely denoting

⋆ E-mail: giuliana.cosentino.15@ucl.ac.uk

© 2017 The Author(s)
Published by Oxford University Press on behalf of the Royal Astronomical Society

Downloaded from https://academic.oup.com/mnras/article/474/3/3760/4662631 by Biblioteca di Scienze tecnologiche user on 29 September 2020

the earliest stages in their evolution as predicted by simulations of molecular cloud formation (Van Loo et al. 2007; Hennebelle et al. 2008; Heitsch, Ballesteros-Paredes & Hartmann 2009). Several scenarios have been proposed to explain the formation of IRDCs, including flow-driven formation, gravitational collapse, and cloud–cloud collisions (e.g. Hennebelle et al. 2008; Heitsch, Ballesteros-Paredes & Hartmann 2009; Tasker & Tan 2009; Van Loo, Keto & Zhang 2014; Wu et al. 2015). Among them, the cloud–cloud collision scenario proposes that IRDCs can form after the collision of already-molecular clouds, and since the collision is expected to be relatively gentle (with velocities from a few to 10 km s^{-1} as opposed for instance to the flow-driven scenario; e.g. Wu et al. 2016, 2017a,b) signatures of the cloud–cloud collision (which involves a large-scale shock interaction) should be observable in the kinematics and excitation of the molecular line spectra observed towards young IRDCs (e.g. Wu et al. 2015).

One of the best tracers of shock interactions in star-forming regions is silicon monoxide (or SiO). This molecule is known to be heavily depleted in the quiescent gas of molecular dark clouds (with measured upper limits to the SiO abundance of $\leq 10^{-12}$; Martin-Pintado, Bachiller & Fuente 1992; Jiménez-Serra et al. 2005), but its abundance is enhanced by up to six orders of magnitude in shocked regions associated with molecular outflows (measured SiO abundances as high as $\sim 10^{-6}$; Martin-Pintado et al. 1992; Jiménez-Serra et al. 2005). SiO is thought to be produced in shocks after the release of Si into the gas phase mainly by the sputtering of dust grains (either from the icy mantles or from the grain cores; see Schilke et al. 1997; Jiménez-Serra et al. 2008). Depending on the velocity of the shock, the SiO emission will show different line profiles: while the SiO gas in high-velocity shocks presents broad line emission red- and blueshifted by tens of km s^{-1}, the SiO emission in low-velocity shocks should be significantly narrower (with line widths $\leq$1–2 km s^{-1}; Jiménez-Serra et al. 2009).

One of the first attempts to detect the signature of a cloud–cloud collision in an IRDC was reported by Jiménez-Serra et al. (2010). In this work, These authors presented the detection of widespread emission of SiO towards the filamentary IRDC G035.39−00.33 (or cloud H in Butler & Tan 2009). The detailed analysis of the SiO line profiles across this cloud revealed two different contributions: (i) a bright and compact component with broad line emission clearly associated with on-going star formation activity; and (ii) a weak, narrow (line widths $\leq$2 km s^{-1}) and extended component detected even towards the most quiescent regions in the IRDC. Among other possibilities, Jiménez-Serra et al. (2010) proposed that the widespread and narrow component of SiO could have been generated by a large-scale cloud–cloud collision related to the origin of the IRDC itself. This cloud indeed shows a complex kinematic structure with several velocity-coherent filaments separated in velocity space by $\sim$3 km s^{-1}, which seem to be interacting (see Henshaw et al. 2013, 2014; Jiménez-Serra et al. 2014). Therefore, the proposed *gentle* shock interaction between the velocity-coherent filaments in G035.39−00.33 may have injected enough Si into the gas phase, yielding narrow SiO line profiles as a distinct chemical signature.

Since this first study, other works have analysed the morphology and kinematics of the line emission of SiO in massive molecular clouds, but mainly targeting regions with on-going star formation (see e.g. the W43 and Cygnus X star-forming regions; Nguyen-Luong et al. 2013; Duarte-Cabral et al. 2014). More recently, Csengeri et al. (2016) performed a spectral line survey of massive clumps located in the Galactic plane, covering different evolutionary stages from IRDCs to ultracompact (UC) H II regions. These authors found that the SiO emission is detected in almost all sources, although the shape of the SiO line profiles clearly varies as a function of evolutionary stage. Indeed, while the most active clumps show line profiles with two clear components (a 20 km s^{-1} wide broad component and a 5–6 km s^{-1} wide narrow component), in the most quiescent sources (mostly associated with IRDCs) only the narrow component is detected. These findings indicate that narrow SiO emission may be a common feature in IRDCs and that it may arise from low-velocity shocks. Unfortunately, Csengeri et al. (2016) carried out single-pointing observations and, therefore, the overall morphology of this narrow SiO emission in other IRDCs remains unknown.

The aim of this work is to extend the study carried out by Jiménez-Serra et al. (2010) in G035.39−00.33 to other IRDCs known to be at a relatively early stage in their evolution (as measured by their low levels of star formation activity). To this purpose, we have carried out large-scale maps of the emission of SiO and methanol (CH_3OH), and of dense gas tracers ($H^{13}CO^+$ and $HN^{13}C$), towards three IRDCs: G028.37+00.07, G034.43+00.24, and G034.77−00.55 (clouds C, F, and G, respectively, following Butler & Tan 2012). Like SiO, CH_3OH is also known to be enhanced in outflows by several orders of magnitude (e.g. L1157 mm and L1448 mm; Bachiller et al. 2001; Jiménez-Serra et al. 2005), and therefore it is a good probe of the interaction of low-velocity shocks. The three clouds of our study belong to the sample of 10 clouds selected by Butler & Tan (2009) from the Rathborne et al. (2006) catalogue. They were selected because they are nearby, massive, and show high contrast compared to the surrounding diffuse emission.

The paper is organized as follows. In Section 2 we provide details about the observations, while in Section 3 we describe the tools and procedures adopted for our data analysis. In Section 4 we present our results on the detection of widespread SiO and CH_3OH emission towards G028.37+00.07, G034.43+00.24, and G034.77−00.55 and analyse their kinematics in detail. In Section 5 we calculate the abundances of SiO and CH_3OH across the clouds, and in Sections 7 and 8 we discuss our results and present our conclusions.

2 OBSERVATIONS

The J = 1 → 0 rotational transitions of $H^{13}CO^+$ and $HN^{13}C$, the J = 2 → 1 line of SiO, and the J = 3 → 2 transitions of CH_3OH were mapped towards the IRDCs G028.37+00.07, G034.43+00.24, and G034.77−00.55 in 2013 May and September using the Instituto de Radioastronomía Milimétrica (IRAM) 30-m telescope in Pico Velata, Spain. For simplicity, hereafter we will refer to G028.37+00.07 as cloud C, G034.43+00.24 as cloud F, and G034.77−00.55 as cloud G. The map sizes were 264 × 252 arcsec^2 for cloud C, 144 × 264 arcsec^2 for cloud F, and 204 × 240 arcsec^2 for cloud G. Maps were obtained using the On-The-Fly (OTF) observing mode with central coordinates at α(J2000) = $18^h42^m52\overset{s}{.}3$, δ(J2000) = $-4°02'26\overset{''}{.}2$ for cloud C, α(J2000) = $18^h53^m18^s$, δ(J2000) = $1°27'22\overset{''}{.}1$ for cloud F, and α(J2000) = $18^h56^m45^s$, δ(J2000) = $1°21'45''$ for cloud G. The off-positions were, respectively, (−370, 30 arcsec), (−200, 0 arcsec), and (−240, −40 arcsec) for clouds C, F, and G, and the angular separation in the direction perpendicular to the scanning direction was 6 arcsec. In Table 1, we report the spectroscopic information of the observed transitions from the Cologne Database for Molecular Spectroscopy (CDMS) catalogue,[1] as well as the beam size and beam efficiency of the IRAM 30-m telescope at these frequencies. (Müller et al. 2005)

[1] See https://www.astro.uni-koeln.de/cdms/catalog.

Downloaded from https://academic.oup.com/mnras/article/474/3/3760/4662631 by Biblioteca di Scienze tecnologiche user on 29 September 2020

Table 1. Observed molecular transitions, frequencies, and beam sizes of the raw data.

Molecule	Transition	Frequency (GHz)	E_{up} (K)	g_{up}	A_{ul} ($\times 10^{-5}$) (s^{-1})	θ (arcsec)	Beam eff.
$H^{13}CO^+$	1–0	86.75429	4.2	3	3.85	28	0.81
$HN^{13}C$	1–0	87.09083	4.2	3	2.38	28	0.81
SiO	2–1	86.84699	6.3	5	2.93	28	0.81
CH_3OH	$3_{1,2}$–$2_{1,1}$	145.13186	35.0	7	1.12	17	0.73
CH_3OH	$3_{-2,2}$–$2_{-2,1}$	145.12639	39.8	7	0.69	17	0.73
CH_3OH	$3_{0,3}$–$2_{0,2}^{++}$	145.10315	13.9	7	1.23	17	0.73
CH_3OH	$3_{-1,3}$–$2_{-1,2}$	145.09737	19.5	7	1.10	17	0.73
CH_3OH	$3_{0,3}$–$2_{0,2}$	145.09371	27.1	7	1.23	17	0.73

For the observations both the Versatile Spectrometer Array (VESPA) and Fourier Transform Spectrometer (FTS) were used. VESPA provided a spectral resolution of 40 kHz, corresponding to a velocity resolution of 0.14 km s^{-1} for $H^{13}CO^+$, $HN^{13}C$, and SiO, and of 0.08 km s^{-1} for CH_3OH. The FTS spectrometer provided a spectral resolution of 190 kHz, corresponding to velocity resolutions of 0.40 km s^{-1} for CH_3OH and 0.70 km s^{-1} for the other molecules. For our analysis, we used the data collected with the VESPA spectrometer for all the maps except for CH_3OH in clouds F and G, for which the FTS data have been used. The peak intensities were measured in units of antenna temperature, T_A^*, and converted into main-beam temperature, T_{mb}, using a beam and forward efficiencies of 0.81 and 0.95 for the 3 mm data and 0.73 and 0.93 for the 2 mm spectra, respectively.

The final data cubes were created using the CLASS software within the GILDAS package.[2] The maps have a spatial resolution of 30 arcsec and a pixel size of 15 × 15 arcsec^2 for SiO, $H^{13}CO^+$, and $HN^{13}C$, and a spatial resolution of 18 arcsec and a pixel size of 9 × 9 arcsec^2 for CH_3OH. For all the data cubes, we used a Gaussian convolving kernel with $\sigma = 6$ arcsec for CH_3OH and $\sigma = 10$ arcsec for all the other tracers. In most cases, the spectra were smoothed in velocity to improve the signal-to-noise ratio of the measured line emission. The final properties of every data cube are listed in Table 2.

3 ANALYSIS METHOD: SCOUSE

As shown by Henshaw et al. (2014, 2016), if the molecular gas in a cloud has multicomponent line profiles, a first moment analysis of the molecular emission only provides the average radial velocity between the different components along the line of sight. Therefore, to study in detail the kinematics of the molecular gas in IRDCs, a multi-Gaussian fitting approach needs to be used in order to isolate the gas motions of the individual velocity components. In our case, we performed multi-Gaussian fitting of all the spectra measured in every data cube using the IDL SCOUSE[3] (Semi-automated multi-COmponent Universal Spectral-line fitting Engine) code recently developed by Henshaw et al. (2016).

SCOUSE is a semi-automated procedure developed to fit large amounts of spectra from single-dish and interferometric data cubes in a systematic and efficient way. As a first step, the tool excludes from the analysis the regions where the line peak intensity is lower than a user-provided threshold. Then, it divides the significant remaining region into several smaller areas called spatial averaging areas (SAAs), whose sizes are also defined by the user. All the spectra contained in an SAA are spatially averaged and the user is required to manually fit the average spectrum. Finally, SCOUSE uses the best-fitting values of the average spectrum as input parameters to perform multi-Gaussian fitting for every single spectrum in an SAA. This procedure is repeated for all the identified SAA. In order to make the final fittings physically consistent, the user is also required to provide tolerance levels for the derived peak line intensity, centroid radial velocity, and line width [full width at half-maximum (FWHM)]. The SCOUSE analysis thus provides information on the peak intensity, centroid radial velocity, and FWHM for all velocity components in all emission lines, and on the measured rms noise level in every spectrum. Other statistical parameters, such as the residual value, χ^2, $\tilde{\chi}^2$ (the χ^2 divided by the number of free parameters), and the Akaike information criterion (AIC; Akaike 1974) are also calculated. All this information has been used to evaluate the distribution in radial velocity and line width of the mapped molecular emission in all the clouds of our sample. For a more detailed discussion on SCOUSE see Henshaw et al. (2016).

4 RESULTS

4.1 The dense gas tracers

In Fig. 1, we report the integrated intensity maps of the $H^{13}CO^+$ (left-hand panels) and $HN^{13}C$ (right-hand panels) emission for clouds C (top), F (middle), and G (bottom). The emission levels (black contours) are superimposed on the H_2 mass surface density maps (in grey-scale) obtained by Kainulainen & Tan (2013). In all the following maps, the names (Butler & Tan 2009, 2012) and positions (black crosses; Butler & Tan 2009 for F8 and F9; Butler & Tan 2012 for all the other cores) are indicated for all cores. In all clouds of our sample, the dense gas tracer emission highlights the filamentary morphology of the clouds, closely following the structure detected in extinction (or defined by the H_2 mass surface density map). For clouds C (integrated velocity range 76–83 km s^{-1}) and F (velocity range 51–64 km s^{-1}), the $H^{13}CO^+$ and $HN^{13}C$ emission shows similar spatial distributions, with peaks mainly associated with the cores present in the clouds.

In contrast to clouds C and F, cloud G (integrated velocity range 39–45 km s^{-1}) shows a slightly different spatial distribution for $H^{13}CO^+$ (left) and $HN^{13}C$ (right). The $HN^{13}C$ emission peaks coincide with the location of the two north-eastern cores G2 and G3, while the $H^{13}CO^+$ emission peaks towards the north-west of the cloud at offset (0, 130 arcsec). The distance between the $HN^{13}C$ and the $H^{13}CO^+$ emission peaks is 54 arcsec (0.76 pc), larger than the angular resolution of our maps (30 arcsec) and enough to conclude that the $H^{13}CO^+$ emission peak is not associated with the two north-eastern cores of the cloud. To the best of our knowledge, no cores are present at the position of the $H^{13}CO^+$ emission peak.

[2] See http://www.iram.fr/IRAMFR/GILDAS.
[3] See https://github.com/jdhenshaw/SCOUSE

Downloaded from https://academic.oup.com/mnras/article/474/3/3760/4662631 by Biblioteca di Scienze tecnologiche user on 29 September 2020

Table 2. Observed molecular transitions, final beam sizes, and velocity resolution of the data cubes used in our analysis.

	Molecule	Beam size (arcsec)	δv (km s^{-1})	rms (K)	δv (kHz)
Cloud C	α(J2000) = 18:42:52.3, δ(J2000) = −4:02:26.2, map size = 264 × 252 arcsec^2				
	$H^{13}CO^+$ (1–0)	30	0.28	0.010	80
	$HN^{13}C$ (1–0)	30	0.28	0.007	80
	SiO (2–1)	30	0.56	0.010	160
	CH_3OH ($3_{0,3}$–$2^{++}_{0,2}$)	18	0.32	0.014	160
	CH_3OH ($3_{-1,3}$–$2_{-1,2}$)	18	0.32	0.014	160
	CH_3OH ($3_{0,3}$–$2_{0,2}$)	18	0.32	0.014	160
Cloud F	α(J2000) = 18:53:18, δ(J2000) = 1:27:22.1, map size = 144 × 264 arcsec^2				
	$H^{13}CO^+$ (1–0)	30	0.14	0.012	40
	$HN^{13}C$ (1–0)	30	0.14	0.011	40
	SiO (2–1)	30	0.56	0.006	160
	CH_3OH ($3_{1,2}$–$2_{1,1}$)	18	0.80	0.005	380
	CH_3OH ($3_{-2,2}$–$2_{-2,1}$)	18	0.80	0.005	380
	CH_3OH ($3_{0,3}$–$2^{++}_{0,2}$)	18	0.80	0.005	380
	CH_3OH ($3_{-1,3}$–$2_{-1,2}$)	18	0.80	0.005	380
	CH_3OH ($3_{0,3}$–$2_{0,2}$)	18	0.80	0.006	380
Cloud G	α(J2000) = 18:56:45, δ(J2000) = 1:21:45.0, map size = 204 × 240 arcsec^2				
	$H^{13}CO^+$ (1–0)	30	0.28	0.011	80
	$HN^{13}C$ (1–0)	30	0.28	0.010	80
	SiO (2–1)	30	0.28	0.011	80
	CH_3OH ($3_{0,3}$–$2^{++}_{0,2}$)	18	0.40	0.008	190
	CH_3OH ($3_{-1,3}$–$2_{-1,2}$)	18	0.40	0.008	190
	CH_3OH ($3_{0,3}$–$2_{0,2}$)	18	0.40	0.008	190

4.1.1 Substructures identification

Visual inspection of the $H^{13}CO^+$ and $HN^{13}C$ spectra throughout each IRDC confirms that a single Gaussian component is a poor approximation to the spectral line profiles observed at certain locations. Each cloud appears to exhibit a dominant velocity component that largely follows the morphology of the IRDC as seen in extinction. For clouds C, F, and G these are situated at ∼79.5, ∼58.5, and ∼41.9 km s^{-1}, respectively. However, each cloud shows additional, morphologically distinct features that are shifted from the dominant component in either position or velocity (or both). These additional features lead to asymmetries in the line profiles of the $HN^{13}C$ and $H^{13}CO^+$ lines. In Fig. 2, $HN^{13}C$ spectra extracted towards different positions across the clouds are displayed. Form this figure, it is clear that the spectra exhibit different central velocities towards different region in the clouds, indicating the presence of multiple velocity structures. These components show differences in the centroid radial velocities >1 km s^{-1}, i.e. more than 2/3 the mean emission line width in all clouds and more than 7× and 3.5× the velocity resolution (δv) for cloud F, and clouds C and G, respectively.

In order to determine the spatial extent and kinematics of these substructures, we further investigate the overall distribution of the central radial velocities and line widths of $H^{13}CO^+$ and $HN^{13}C$ extracted using SCOUSE across the clouds. In Fig. 3, we show histograms of the velocity distributions obtained for $H^{13}CO^+$ (left-hand panels, in red) and $HN^{13}C$ (right-hand panels, in blue) towards clouds C (top), F (middle), and G (bottom). The bin size in the x-axis corresponds to 1/3 of the mean intensity-weighted line width, obtained from the SCOUSE results (see Section 4.1.2 and Table 6). This corresponds to 0.5 km s^{-1} for the three clouds. In the y-axis we plot the percentage of emission line components having central velocities falling within the bin. For each histogram, we also report the mean uncertainty on the central velocity, obtained by averaging the central velocity uncertainties derived by SCOUSE for each fitted line component.

Asymmetries in the distribution of the radial velocities for each cloud are more pronounced in Fig. 3. The velocity distribution of $H^{13}CO^+$ and $HN^{13}C$ is best fitted with three Gaussians (black lines). Using $HN^{13}C$ (right-hand panels), where the asymmetries are most prominent, we define a velocity range for each cloud component as follows:

$$\Delta V = V_{\rm LSR}^{\rm gf} \pm (1.5\,\sigma^{\rm gf}), \quad (1)$$

where ΔV is the velocity range of the substructures, $V_{\rm LSR}^{\rm gf}$ is the central velocity and $\sigma^{\rm gf}$ the standard deviation of the fitted Gaussian (gf = Gaussian fitting). In Table 3, we report the velocity ranges defined for the substructures and their mean velocities obtained as (Jiménez-Serra et al. 2014)

$$\langle V \rangle = \frac{\Sigma_i V_i I_i}{\Sigma_i I_i}. \quad (2)$$

The goodness of fit is provided by calculating the mean of the main residual values defined as

$$\text{Mean residual} = \frac{\Sigma |G_i - (N/N_{\rm tot})_i|}{N_{\rm bin}}, \quad (3)$$

where G_i indicates the value of the multi-Gaussian fitting at the ith bin, $(N/N_{\rm tot})_i$ is the number of fitted lines falling within the ith bin, and $N_{\rm bin}$ is the number of bins of the histogram.

Since both $H^{13}CO^+$ and $HN^{13}C$ are predominantly tracers of high-density material, and each component is well separated in velocity (Fig. 3), the chances of confusion and/or blending between components are small. However, we note that a more comprehensive description of the gas kinematics of each cloud using more abundant,

Downloaded from https://academic.oup.com/mnras/article/474/3/3760/4662631 by Biblioteca di Scienze tecnologiche user on 29 September 2020

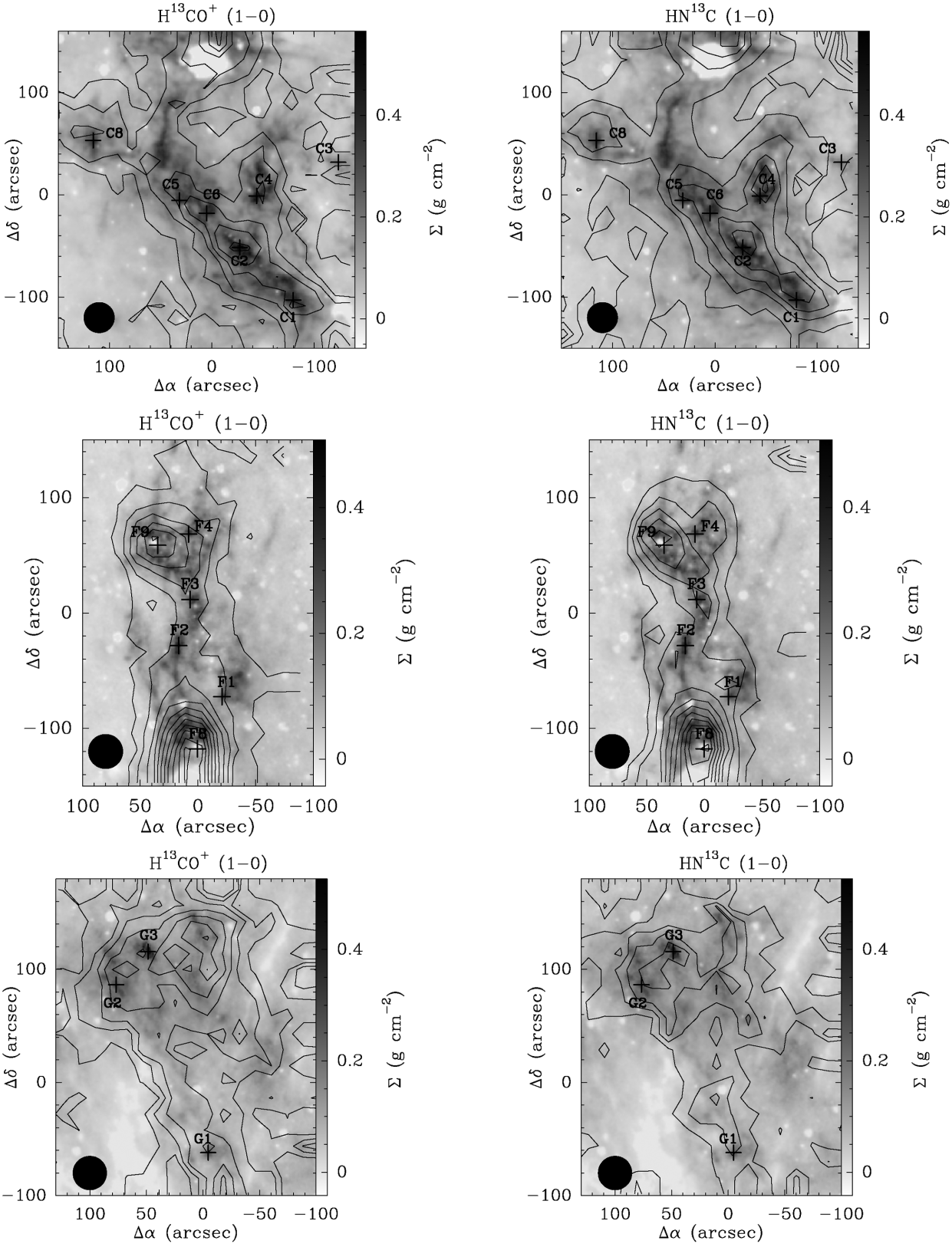

Figure 1. Integrated intensity maps of the $H^{13}CO^+$(1–0) (left) and $HN^{13}C$(1–0) (right) lines towards clouds C (top panels), F (middle panels), and G (bottom panels). Emission levels (black contours), from 3σ by 3σ, are superimposed on the H_2 mass surface density maps (grey-scale) obtained by Kainulainen & Tan (2013). Cloud C: the integration range is 76–83 km s^{-1} and $\sigma = 0.10$ K km s^{-1} for both molecules. Cloud F: integration range is 51–64 km s^{-1} for both tracers and $\sigma = 0.11$ and 0.15 K km s^{-1} for $H^{13}CO^+$ and $HN^{13}C$, respectively. Cloud G: integration range is 39–45 km s^{-1} and $\sigma = 0.09$ and 0.06 K km s^{-1} for $H^{13}CO^+$ and $HN^{13}C$, respectively. The core positions (black crosses; Butler & Tan 2009, 2012) and the beam sizes (black circles) are shown in all panels.

Downloaded from https://academic.oup.com/mnras/article/474/3/3760/4662631 by Biblioteca di Scienze tecnologiche user on 29 September 2020

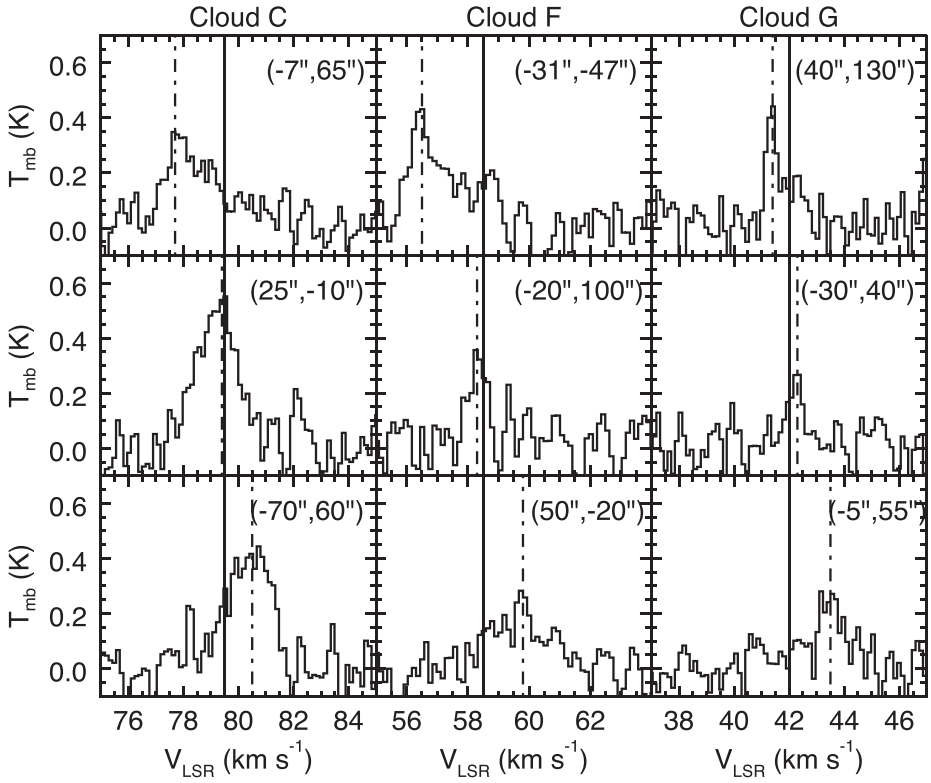

Figure 2. $HN^{13}C$ spectra for clouds C (left-hand panel), F (middle panel), and G (right-hand panel) extracted towards several positions and highlighting the presence of multiple velocity components. The vertical solid lines correspond to the central velocity of the clouds, while the vertical dot–dashed lines indicate the central velocity of the spectrum peaks. The same result has been found for the $H^{13}CO^+$ emission in all the three clouds and are not shown for simplicity.

lower density gas tracers, and more sophisticated techniques (see Henshaw et al. 2014), will be presented in two forthcoming papers (Barnes et al., in preparation; Henshaw et al., in preparation).

These substructures can be visualized in Fig. 4 where we show the integrated intensity maps obtained for $HN^{13}C$ for the velocity ranges given in Table 3. The identified substructures have filamentary shapes and change in position as a function of velocity with respect to the IRDC seen in extinction. In particular, for cloud C (uppermost panels) the central and brightest substructure at 79.5 km s^{-1} extends from south-west to north, following the structure of the cloud. The blueshifted substructure with mean velocity 77.8 km s^{-1} (uppermost left-hand panel), however, is fainter and its emission arises mainly from the eastern part of the cloud peaking at cores C5, C2, and C1. The redshifted substructure peaking at 81.4 km s^{-1} (uppermost right-hand panel) shifts towards the western part of the cloud and runs from the south-west to the north-west exhibiting an arch-like shape. Its emission seems to be associated with cores C4 and C1. The three substructures spatially overlap towards the central chain of cores. A similar behaviour was also noted for IRDC G035.39−00.33 (or cloud H) by Jiménez-Serra et al. (2014). For cloud F (Fig. 4, middle panels), the blueshifted substructures with mean velocity 56.6 km s^{-1} (left-hand panel) is the faintest, least extended, and arises mainly from the western part of the cloud. As we move to more redshifted velocities, the central elongated substructure at 58.5 km s^{-1} becomes apparent (middle panel), showing the brightest emission and following the filamentary structure of the cloud seen in the H_2 mass surface density map. The redshifted substructure peaking at 59.5 km s^{-1} (right-hand panel) is also elongated but the bulk of the emission shifts towards the east of the cloud.

Very peculiar is the spatial distribution of the substructures in cloud G (bottom panels in Fig. 4). The blueshifted substructures centred at 41.0 km s^{-1} (left-hand panel) is the least extended and its emission clearly originates from the G3 core. This is also true for the central substructure at 41.9 km s^{-1} (middle panel), although it shows two extensions towards the south-west following the H_2 mass surface density map.

In contrast, the redshifted substructure of cloud G at 43.5 km s^{-1} (right-hand panel) shows a U-shape facing north-east unseen in the other substructures.

4.1.2 *Line width distribution*

We now investigate whether the velocity components of the dense gas show any difference in their measured line widths. In Fig. 5, we report the line width distributions for both $HN^{13}C$ (in blue) and $H^{13}CO^+$ (in red) observed towards clouds C (top panel), F (middle panel), and G (bottom panel). The bin size has been evaluated as in Fig. 3 and the percentage of emission lines having line widths falling in every bin are shown in the *y*-axis. For each histogram, we report the mean uncertainty in the line width, derived averaging the uncertainty in all the line widths derived by SCOUSE. From Fig. 5, we find a smooth distribution that peaks between 1 and 2 km s^{-1} with no multiple line width components. The line widths for both molecules are in any case narrower than 5 km s^{-1}.

The overall intensity-weighted average line width, and the average line width of each substructure found in the three clouds, can be calculated as (Jiménez-Serra et al. 2014)

$$\langle \Delta v \rangle = \frac{\Sigma_i \Delta v_i I_i}{\Sigma_i I_i}, \quad (4)$$

Downloaded from https://academic.oup.com/mnras/article/474/3/3760/4662631 by Biblioteca di Scienze tecnologiche user on 29 September 2020

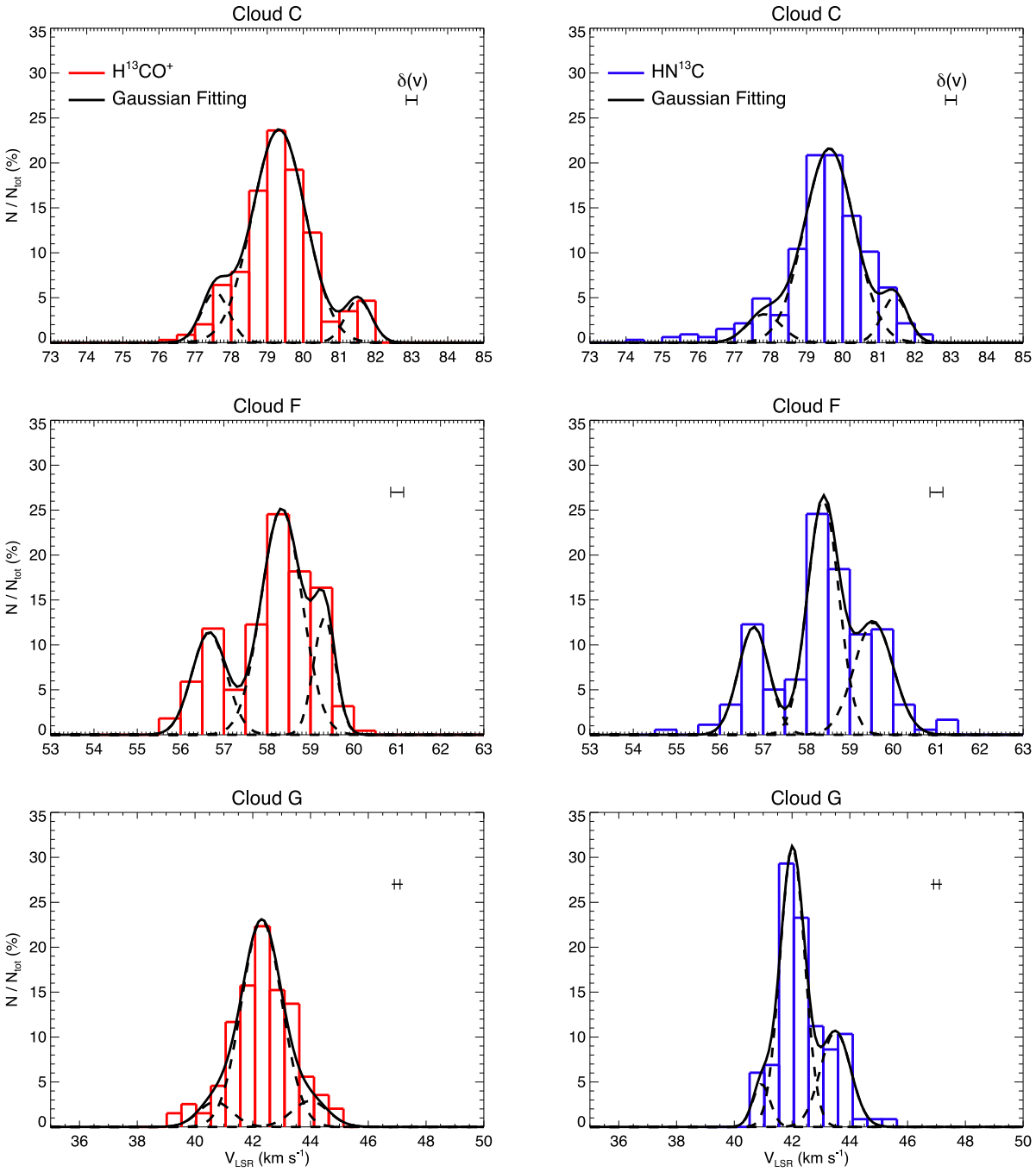

Figure 3. Velocity distributions of the $H^{13}CO^+$ (red) and $HN^{13}C$ (blue) emissions as obtained for cloud C (top panel), cloud F (middle panel), and cloud G (bottom panel). The histograms show the percentage of emission lines having V_{LSR} falling within the δV of the bin. Bin sizes are 0.5 km s^{-1} for the three clouds, which corresponds to 1/3 of mean intensity-weighted line width for the two tracers. In all panels the mean uncertainty in the central velocities of the fittings is indicated.

where Δv is line width and I_i is the intensity measured for each velocity component in each position of the data cube. The obtained values are listed in Table 6.

From Table 6, the difference between the average line width of $H^{13}CO^+$ and $HN^{13}C$ is always $<2\,\delta v$ for the three clouds, which implies that the dynamics of ion species is not significantly different from that of neutral molecules. Therefore, although these differences have been reported in more evolved high-mass star-forming regions (as e.g. DR21; see Hezareh et al. 2010), we do not find any evidence for this phenomena in the quiescent gas of IRDCs.

4.2 Shock tracer emission: SiO and CH_3OH

In Fig. 6, the integrated intensity maps obtained for the shock tracers SiO and CH_3OH are shown. The emission levels for SiO (right-hand panels) and CH_3OH (left-hand panels) are superimposed on the H_2 mass surface density maps of Kainulainen & Tan (2013, in grey-scale). Sample spectra extracted from different positions across clouds C (top panel), F (middle panel), and G (bottom panel) are also presented in Fig. 7 to illustrate the change in line width and velocity across the clouds.

Downloaded from https://academic.oup.com/mnras/article/474/3/3760/4662631 by Biblioteca di Scienze tecnologiche user on 29 September 2020

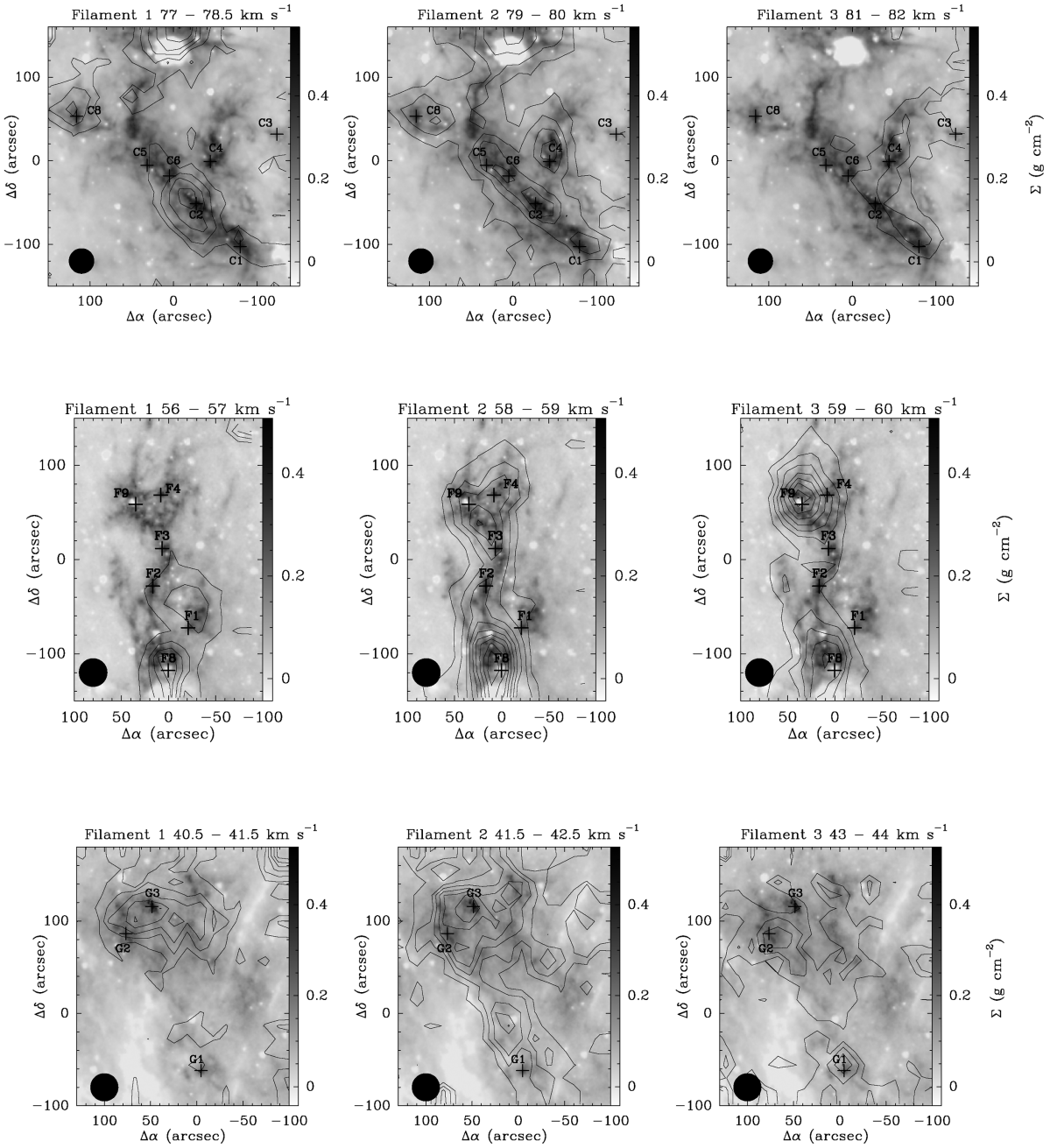

Figure 4. Integrated intensity maps of the $HN^{13}C$ emission in clouds C (top panels), F (middle panels), and G (bottom panels) for the identified velocity substructures. The emission levels (black contours) are superimposed on the H_2 mass surface density map of Kainulainen & Tan (2013). The integrated velocity ranges are indicated in every panel and the emission levels go from 3σ by 3σ, where $\sigma = 0.04$ K km s^{-1} for cloud C, $\sigma = 0.04$ K km s^{-1} for cloud F, and $\sigma = 0.02$ K km s^{-1} for cloud G. The beam sizes are shown as black circles in all panels.

For simplicity, we only show the integrated intensity map obtained for the $3_{0,3} \rightarrow 2_{0,2}$ CH_3OH transition.

4.2.1 Shock tracer emission in clouds C and F

From Fig. 6, we find that the SiO and CH_3OH emission detected towards clouds C and F is bright and widespread over several parsecs (spatial extent of 4.8×6.8 pc^2 for SiO and 6.3×6.8 pc^2 for CH_3OH towards cloud C, and spatial extent of 2.3×4.8 pc^2 for both SiO and CH_3OH towards cloud F). For cloud C (top panels), SiO is mainly associated with the massive cores in the cloud, especially those located along the central ridge known to be actively forming massive stars (see Wang et al. 2011; Zhang et al. 2014). The CH_3OH emission is also bright towards the same regions where SiO is detected, although it shows an additional extension towards the northern quiescent parts of cloud C such as the emission towards C8 and the emission between C5 and the northern, very bright, infrared source (see 3σ contour in the top left-hand panel), following the morphology of the IRDC, and which remains unseen in SiO.

For cloud F (middle panels), the emission of both SiO and CH_3OH shows a similar pattern to that observed in cloud C. The brightest emission peaks of SiO and CH_3OH coincide with the

Downloaded from https://academic.oup.com/mnras/article/474/3/3760/4662631 by Biblioteca di Scienze tecnologiche user on 29 September 2020

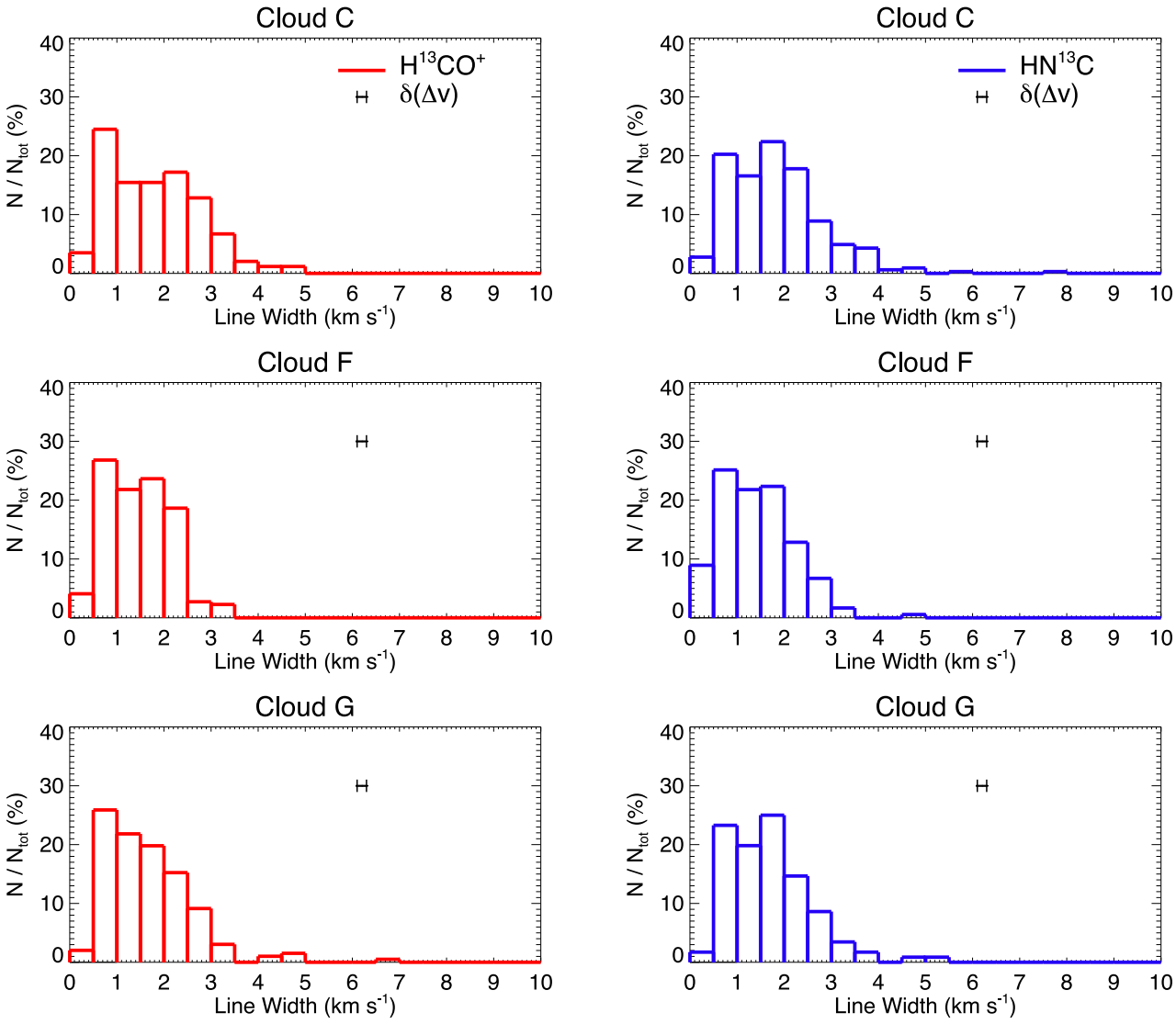

Figure 5. Line width distributions of the $H^{13}CO^+$ (left-hand panels in red) and $HN^{13}C$ (right-hand panels in blue) emission measured for clouds C (top panels), F (middle panels), and G (bottom panels). The histograms show the percentage of emission lines having line widths falling within each bin. Bin sizes are 0.5 km s^{-1} for the three clouds, corresponding to 1/3 of the mean intensity-weighted line width. In each panel the mean uncertainty in the line width of the single fittings is indicated.

location of two active massive star-forming cores F8 and F9 (see Rathborne et al. 2009, 2011), while the third SiO and CH_3OH peak, at offset (−35, −20 arcsec), is just 0.43 pc away from the low-mass star-forming cluster identified by Foster et al. (2014), offset (−17, −40 arcsec). It is then very likely that this third SiO and CH_3OH emission peak is associated with this star-forming cluster. As with cloud C, note that an additional extension is detected in CH_3OH with respect to SiO towards the central regions of cloud F (see 3σ contour in the middle left-hand panel), coinciding with the most quiescent regions and cores in this cloud, such as core F2.

4.2.2 *The case of cloud G*

Very peculiar is the spatial distribution of the SiO and CH_3OH emission in cloud G (Fig. 6, bottom panels). Unexpectedly, the SiO emission detected towards this cloud appears concentrated towards the north-west at a location off the cloud with a visual extinction of just $A_v \sim 20$–30 mag [at offset (−28, 103 arcsec)], corresponding to a mass surface density of 0.06–0.09 g cm^{-2}, and far away from the massive cores reported in this cloud. This is also true for the brightest emission of CH_3OH detected in cloud G [offset (−15, 110 arcsec)], as if both molecules had been enhanced by the same mechanism towards this position. We note however that, in contrast to SiO, CH_3OH is extended across the whole cloud and spatially follows the most quiescent regions in the IRDC (see Fig. 6). Therefore, the spatial distribution of the shock tracers SiO and CH_3OH in cloud G shows that *their emission peaks are completely offset from the known massive cores in the cloud, and that the SiO emission does not follow the morphology of the dense gas.*

4.2.3 *The broad and narrow components*

By using SCOUSE and following a procedure similar to that performed for the dense gas tracers, in Fig. 8 we present the line width distribution for SiO (in green) and CH_3OH (in orange) towards clouds C (top panels), F (middle panels), and G (bottom panels).

Downloaded from https://academic.oup.com/mnras/article/474/3/3760/4662631 by Biblioteca di Scienze tecnologiche user on 29 September 2020

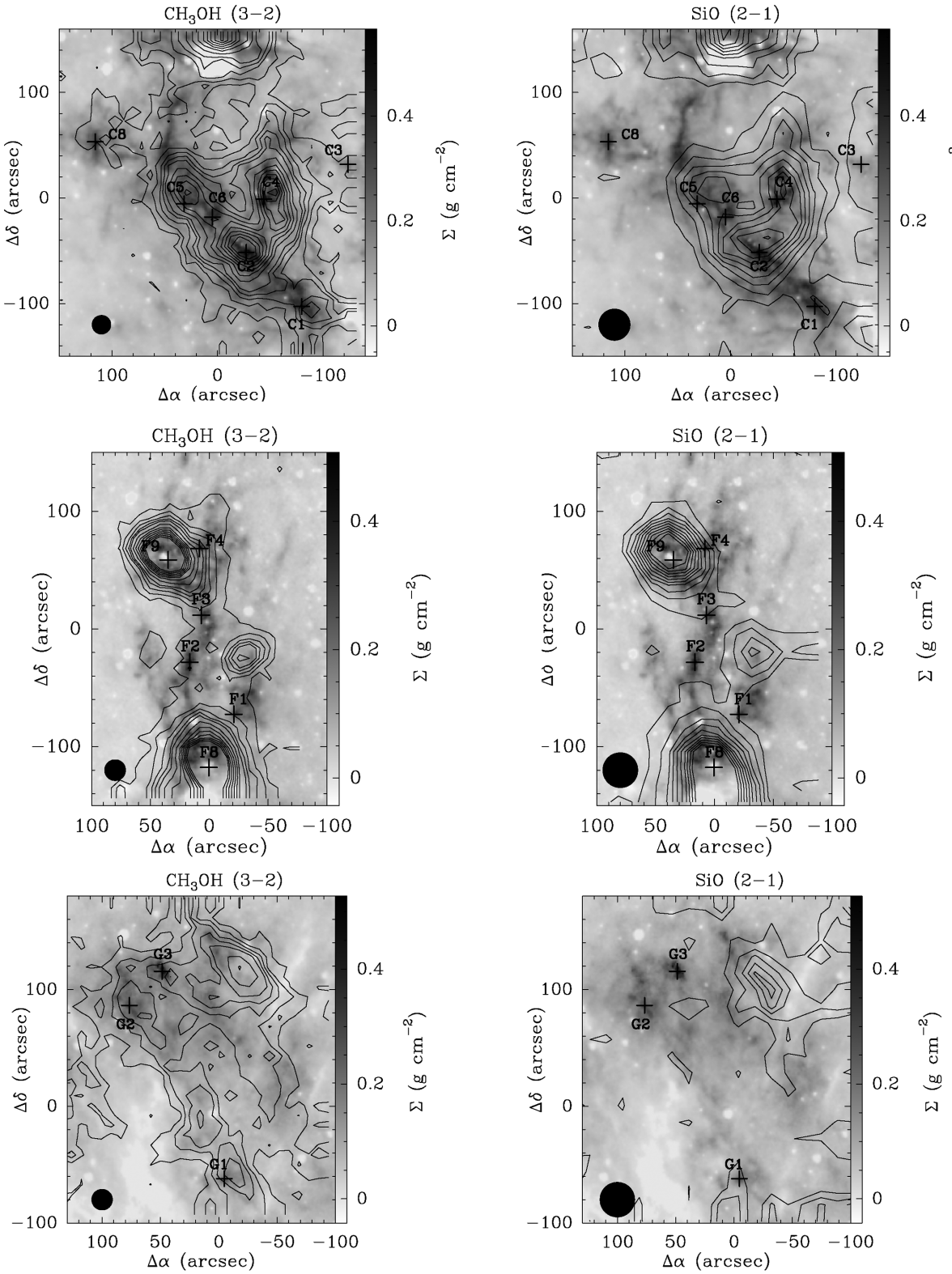

Figure 6. Integrated intensity maps of the CH_3OH(3–2) (left) and SiO(2–1) (right) lines towards clouds C (top panels), F (middle panels), and G (bottom panels). Emission levels (black contours) are 3σ, 6σ, 9σ, 12σ, 15σ, 21σ, 27σ, 33σ, 39σ, 45σ, 51σ, and 57σ for CH_3OH; 3σ, 6σ, 9σ, 12σ, 15σ, 18σ, 21σ, 24σ, 27σ, and 30σ for SiO. The contours are superimposed on the H_2 mass surface density maps (grey-scale) obtained by Kainulainen & Tan (2013). Cloud C: the integration ranges are 65–90 km s^{-1} for SiO and 75–85 km s^{-1} for CH_3OH and $\sigma = 0.20$ K km s^{-1} for both molecules. Cloud F: the integration ranges are 40–80 km s^{-1} for SiO and 52–64 km s^{-1} for CH_3OH; $\sigma = 0.24$ and 0.25 K km s^{-1} for SiO and CH_3OH, respectively. Cloud G: integration ranges are 35–50 km s^{-1} for SiO and 38–50 km s^{-1} for CH_3OH; $\sigma = 0.10$ and 0.20 K km s^{-1} for SiO and CH_3OH, respectively. The core positions (black crosses; Butler & Tan 2009, 2012) and the beam sizes (black circles) are shown in all panels.

Downloaded from https://academic.oup.com/mnras/article/474/3/3760/4662631 by Biblioteca di Scienze tecnologiche user on 29 September 2020

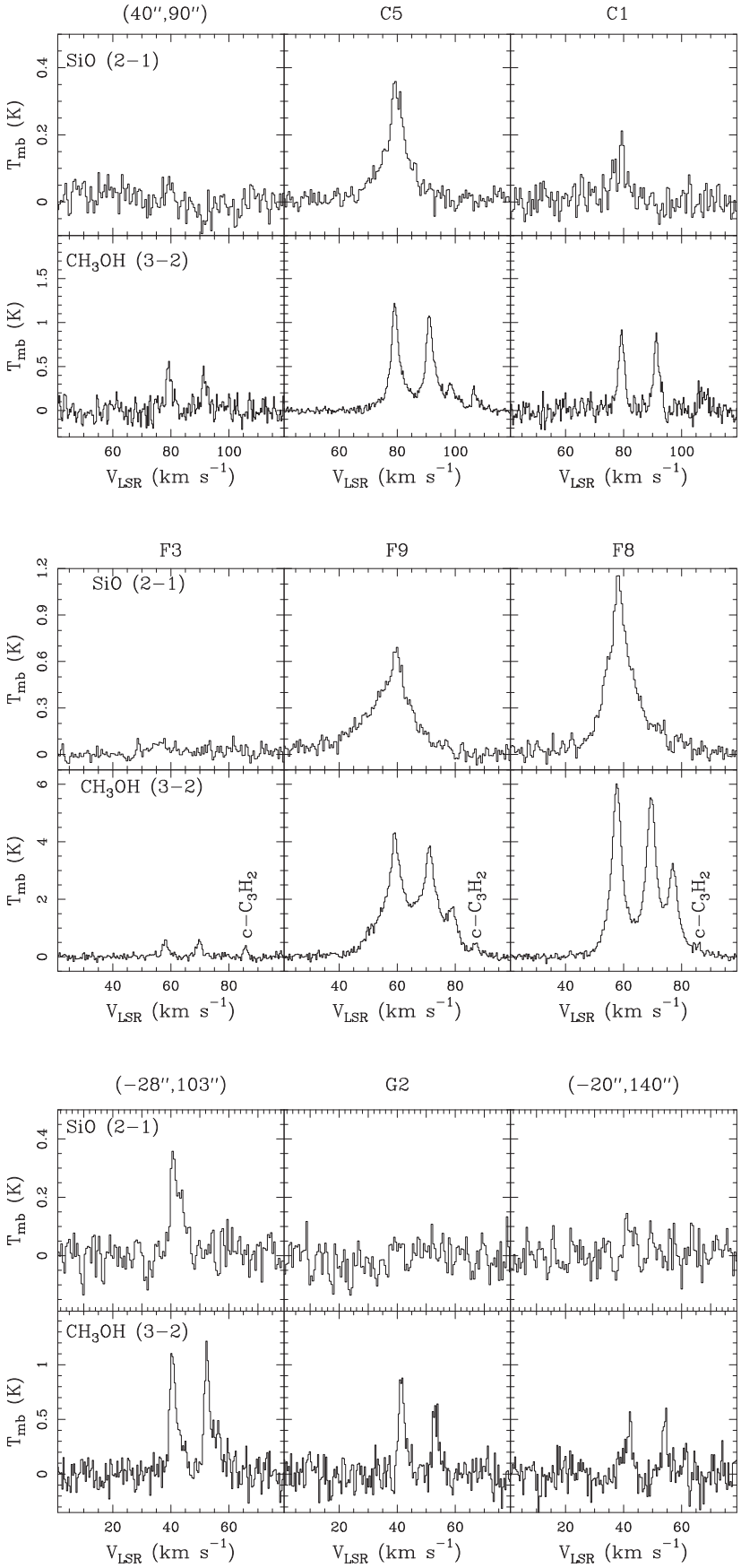

Figure 7. SiO and CH_3OH spectra extracted towards three positions in clouds C (top panel), F (middle panel), and G (bottom panel). The corresponding position is indicated for every spectrum.

Downloaded from https://academic.oup.com/mnras/article/474/3/3760/4662631 by Biblioteca di Scienze tecnologiche user on 29 September 2020

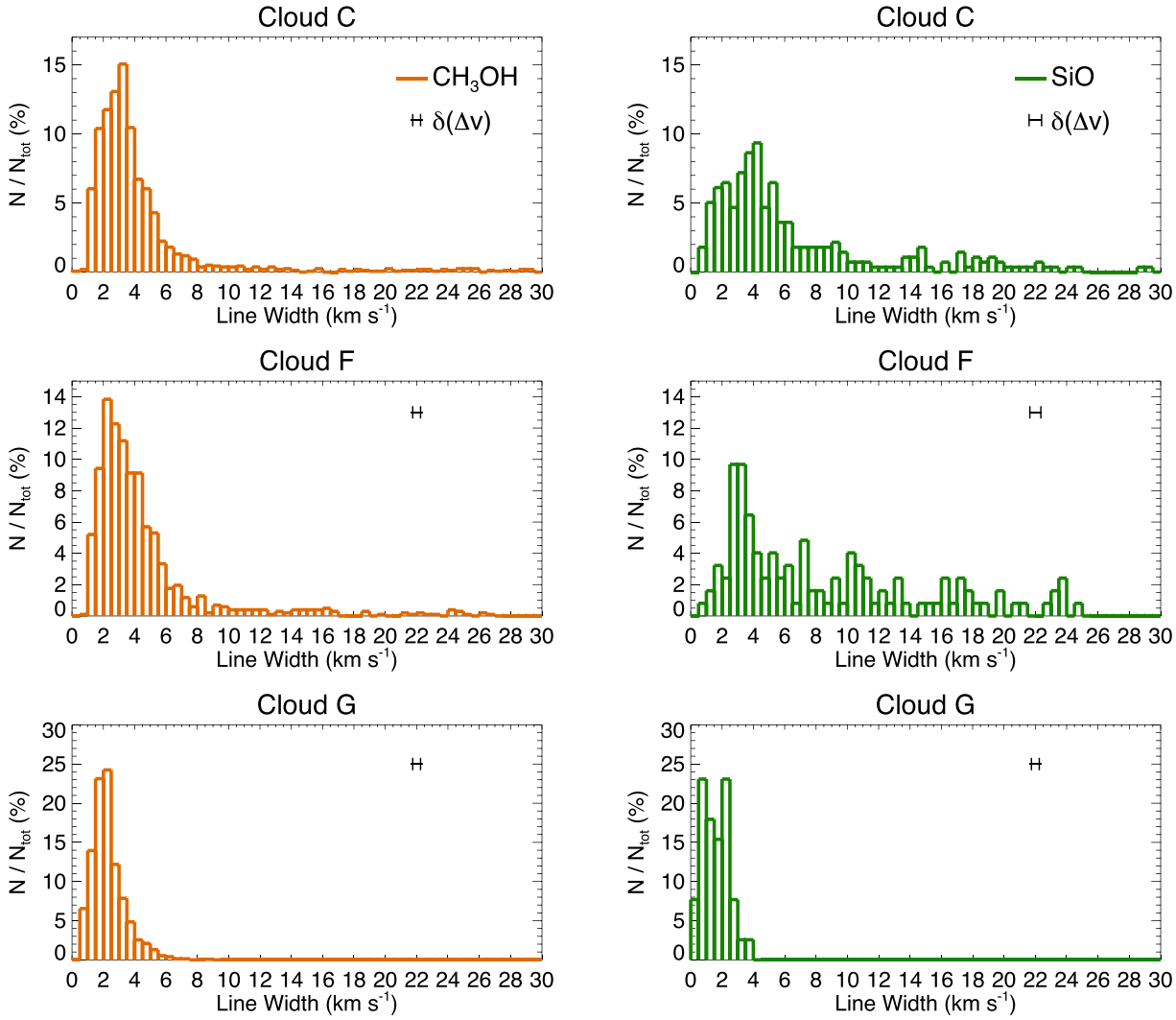

Figure 8. Line width distributions of the CH_3OH (in orange) and SiO (in green) emissions obtained for clouds C (top panels), F (middle panels), and G (bottom panels). The histograms show the percentage of emission lines having line widths falling within each bin. Bin size for the CH_3OH and SiO distributions is 0.5 km s^{-1} corresponding to 1/3 of the mean intensity-weighted line width obtained for the dense gas tracers. In each panel the mean uncertainty in the line widths from the single fittings is indicated.

The bin size in the *x*-axis is 1/3 of the mean intensity-weighted line width obtained for the dense gas tracers (i.e. 0.5 km s^{-1}). This allows us to have a direct comparison between the distributions of SiO/CH_3OH and $HN^{13}C/H^{13}CO^+$. In the *y*-axis we plot the percentage of emission lines having line widths falling within the bin size. For each histogram, we report the mean uncertainty on the line width, derived by averaging the uncertainty in all the line widths obtained by SCOUSE. The CH_3OH histograms have been obtained considering the contributions from the transitions $3_{0,3} \rightarrow 2^{++}_{0,2}$, $3_{-1,3} \rightarrow 2_{-1,2}$, and $3_{0,3} \rightarrow 2_{0,2}$, which have been detected in all clouds. The fraction of velocities in each bin has been obtained considering the velocities obtained for the three transitions and then dividing by the total number of positions (i.e. the sum of the number of significant positions for each transition).

From Fig. 8, we find that the line width distributions of both SiO and CH_3OH for clouds C and F show two main contributions: a narrow component with a well-defined peak at line widths between 2 and 4 km s^{-1}, and a more distributed broader component with line widths up to 30 km s^{-1}. In contrast to clouds C and F, the line width distribution obtained for cloud G only shows the narrow component for both SiO and CH_3OH with typical line widths $\leq$3 km s^{-1}. From the line width distributions in Fig. 8 only, it is difficult to define a clear threshold between the two components. Hence, we use the line width distribution of the high-density tracers $H^{13}CO^+$ and $HN^{13}C$ to define such as threshold (see Fig. 5), since their emission is not affected by shocks. Since the line widths from $H^{13}CO^+$ and $HN^{13}C$ are narrower than 5 km s^{-1}, we thus establish the threshold between narrow and broad SiO and CH_3OH components at 5 km s^{-1}. In Table 4, we report the percentage of SiO and CH_3OH lines having $\Delta v < 5$ km s^{-1}.

From Table 4, it is clear that almost 100 per cent of the SiO and CH_3OH emission in cloud G is narrow, and therefore this component dominates the shock tracer emission in this cloud. On the other hand, the narrow emission in clouds C and F accounts for 45–60 per cent of the SiO emission and 80–85 per cent of CH_3OH measured in these clouds. We note that this difference is even greater when considering a threshold of 3 km s^{-1}, for which the fraction of SiO and CH_3OH narrow emission in cloud G is $\geq$83 per cent, while it

Downloaded from https://academic.oup.com/mnras/article/474/3/3760/4662631 by Biblioteca di Scienze tecnologiche user on 29 September 2020

Table 3. Mean intensity-weighted radial velocities and velocity ranges of the identified substructures in clouds C, F, and G. The mean residual of the multi-Gaussian fitting is reported as indication of fitting goodness.

Cloud	V_1 (km s^{-1})	ΔV_1 (km s^{-1})	V_2 (km s^{-1})	ΔV_2 (km s^{-1})	V_3 (km s^{-1})	ΔV_3 (km s^{-1})	Mean residual
C	77.8	77–78.5	79.5	79–80	81.4	81–82	0.30
F	56.6	56–57	58.5	58–59	59.5	59–60	0.13
G	41.0	40.5–41.5	41.9	41.5–42.5	43.5	43–44	0.13

Table 4. Frequency of detection, in percentages, of the SiO and CH_3OH narrow emission towards clouds C, F, and G, for thresholds <3 and 5 km s^{-1}.

	<3 km s^{-1}			<5 km s^{-1}		
	C (%)	F (%)	G (%)	C (%)	F (%)	G (%)
SiO	28.9	25.8	97.4	62.1	45.2	100
CH_3OH	47.7	46.7	83.4	81.0	85.6	99.9

accounts for 25–50 per cent in clouds C and F. Hence, we conclude that while two line width components (narrow and broad) are clearly identified in clouds C and F, only the narrow component is observed in cloud G. This is clear in Fig. 7 where SiO and CH_3OH spectra, extracted across the three clouds, are shown. In clouds C and F, the SiO and CH_3OH emission has line width $\geq$10 km s^{-1} in positions corresponding to the active cores (see C5 in cloud C and F9 in cloud F), while in the more quiescent regions (see offset (40, 90 arcsec) in cloud C and core F3 in cloud F) the emission line width is as narrow as 5 km s^{-1} or not detected. In cloud G (bottom right-hand panels), the very broad component found in clouds C and F is not detected and even towards the SiO and CH_3OH peaks [see offset (−28, 103 arcsec)] the emission is $\leq$4 km s^{-1}.

4.2.4 *Velocity distribution*

We now investigate the distribution of the radial velocities of the two line width components (broad and narrow) detected in SiO and CH_3OH towards the three clouds. Figs 9 and 10 present the velocity distribution of the broad (orange, left-hand panels) and narrow (green, right-hand panels) emission of, respectively, SiO and CH_3OH. We compare these velocity distributions with the Gaussian fitting obtained for the high-density tracer $HN^{13}C$ (black curves; see also Fig. 3). The velocity distribution of the narrow (broad) component is divided by the number of positions in which the total narrow (broad) emission has been detected.

From Figs 9 and 10, it is clear that the SiO and CH_3OH broad components in clouds C and F show significant emission distributed across a wide range in central velocities. Furthermore, the velocity distributions are clearly unrelated to the velocity substructure identified from the dense gas (as probed by $H^{13}CO^+$ and $HN^{13}C$), and they do not show any coherent substructures by themselves. For cloud G, however, the SiO emission does not show any broad component at all, while the CH_3OH broad component corresponds to just 0.1 per cent of the total emission and its line width is always <6 km s^{-1}.

As shown in Figs 9 and 10, the narrow component is detected in all clouds and, in general, it arises mainly from the main (brightest) substructures detected in $H^{13}CO^+$ and $HN^{13}C$. This indicates that the narrow component is moving as a whole at the central velocity of the corresponding cloud. One exception is found for the SiO narrow emission towards cloud G (right bottom panel in Fig. 9), for which the emission appears skewed to blueshifted velocities. Note that the SiO velocity distribution for the narrow component in cloud F also shows a blueshifted peak centred at ∼56 km s^{-1} (see right middle panel in Fig. 9). This component is associated with core F8 located towards the south of cloud F (see Fig. 6), whose dense gas tracer emission also peaks at this blueshifted velocity. However, unlike the narrow, blueshifted SiO emission in cloud G, the SiO line profiles towards core F8 show both narrow and broad velocity components (see Fig. 7), indicating that the kinematics of the SiO gas in core F8 are driven by active star formation activity.

5 ABUNDANCE OF SiO AND CH_3OH IN IRDCs

In this section, we estimate the abundance of the shock tracers SiO and CH_3OH measured for the narrow and broad components in the three clouds. The presence of several transitions allowed us to perform a multiline excitation analysis for CH_3OH and estimate the excitation temperature, T_{ex}, and total column density, N_{tot}, for this molecule. In order to evaluate these quantities we regridded the CH_3OH data to the largest beam size used in our observations (30 arcsec) and extract spectra towards four positions in each cloud. The selected positions show either the broad or the narrow component and are representative of both the star-forming and quiescent gas. These positions are C1, C2, C8, and offset (40, 90 arcsec) for cloud C; F2, F8, F9, and offset (−30, −20 arcsec) for cloud F; and G1, G2, G3, and offset (−28, 103 arcsec) for cloud G. Assuming the gas being in local thermodynamic equilibrium (LTE) conditions and the emission more extended than the beam size (filling factor ∼1), we used the new software MADCUBAIJ (Rivilla et al. 2016) to calculate T_{ex} and N_{tot} of the narrow CH_3OH emission towards the selected positions. The derived T_{ex} are in the range 6–11 K for all the clouds (see Table 5), similar to those obtained from N_2H^+ and CO observations (see e.g. Henshaw et al. 2014; Jiménez-Serra et al. 2014). The estimated N_{tot} (CH_3OH) lie in the range 3.5×10^{13}–5.8×10^{14} cm^{-2} for cloud C, 3.2×10^{13}–2.4×10^{15} cm^{-2} for cloud F, and 9.8×10^{13}–1.9×10^{14} cm^{-2} for cloud G.

A similar analysis is not possible for SiO, since only one transition was covered in our observations. Hence, in order to estimate the total column density of this molecular species we assumed the T_{ex} derived from CH_3OH in each position and used MADCUBAIJ to calculate the corresponding N_{tot}(SiO) (see Table 5). Towards cores F2, C8, G1, G2, and G3, no SiO emission was detected. Hence, only 3σ upper limits to the abundance of this

Downloaded from https://academic.oup.com/mnras/article/474/3/3760/4662631 by Biblioteca di Scienze tecnologiche user on 29 September 2020

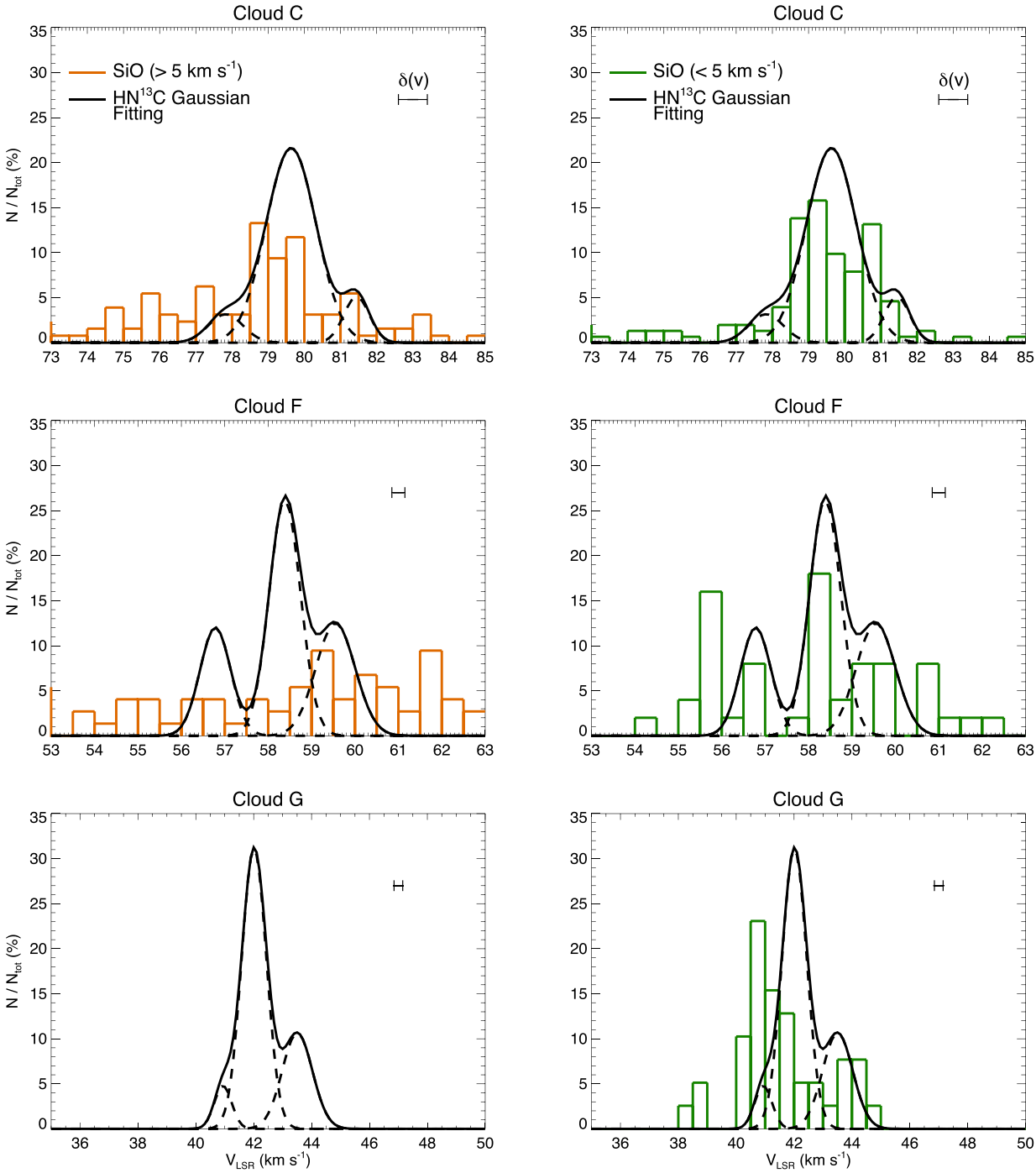

Figure 9. Velocity distribution of the SiO broad (with line widths $>5\,\mathrm{km\,s^{-1}}$, orange in left-hand panels) and narrow (with line widths $<5\,\mathrm{km\,s^{-1}}$, green in right-hand panels) emission obtained for clouds C (top panels), F (middle panels), and G (bottom panels). The histograms show the percentage of emission lines having radial velocities falling within each bin, where the bin size is $0.5\,\mathrm{km\,s^{-1}}$ for the three clouds, corresponding to 1/3 of the mean intensity-weighted line width obtained for the dense gas tracers. In each panel, the mean uncertainty for the central velocities of the single fittings is indicated. Black curves correspond to the Gaussian fitting obtained for $HN^{13}C$ in Section 4.1.1 (see also Fig. 3).

molecule have been estimated. The obtained $N_{\rm tot}$(SiO) are in the range $\leq 3.0\times10^{11}$–$7.4\times10^{12}\,\mathrm{cm^{-2}}$ for cloud C, $\leq 2.5\times10^{11}$–$5.4\times10^{13}\,\mathrm{cm^{-2}}$ for cloud F, and $\leq 2.9\times10^{11}$–$3.3\times10^{12}\,\mathrm{cm^{-2}}$ for cloud G.

In order to evaluate the enhancement of SiO in the narrow component of clouds C, F, and G, we use the emission of $H^{13}CO^+$ as a probe of the H_2 column density and calculate the column density ratio $N(\mathrm{SiO})/N(\mathrm{H^{13}CO^+})$. The abundance of narrow SiO and CH_3OH is estimated as follows:

$$\chi(\mathrm{SiO}) = \frac{N_{\rm tot}(\mathrm{SiO})}{N_{\rm tot}(\mathrm{H^{13}CO^+})}\frac{^{13}\mathrm{C}}{^{12}\mathrm{C}}\chi(\mathrm{HCO^+}), \quad (5)$$

Downloaded from https://academic.oup.com/mnras/article/474/3/3760/4662631 by Biblioteca di Scienze tecnologiche user on 29 September 2020

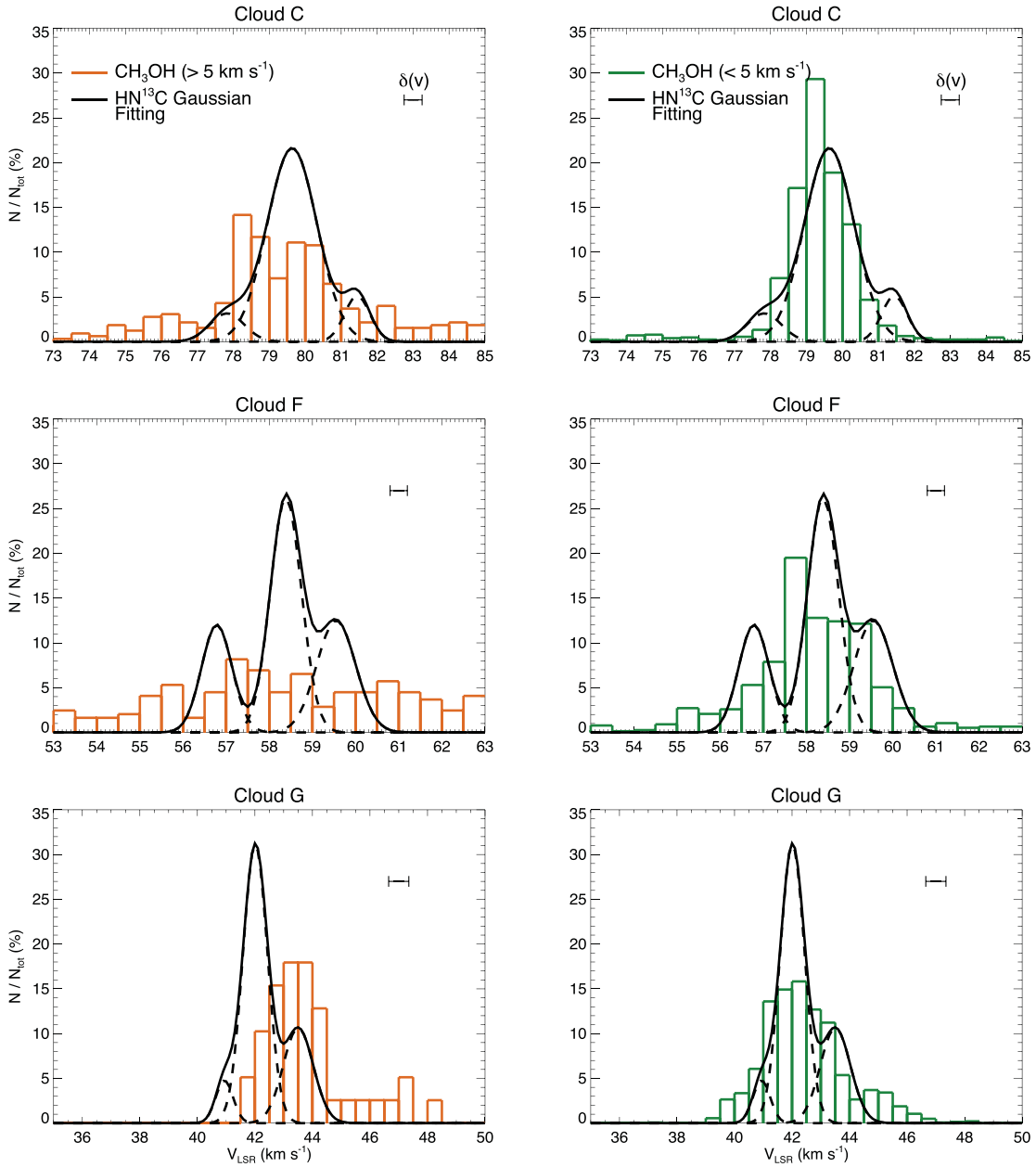

Figure 10. Velocity distribution of the CH_3OH broad (line widths $>5\,km\,s^{-1}$, orange in left-hand panels) and narrow (line widths $<5\,km\,s^{-1}$, green in right-hand panels) emission obtained for clouds C (top panels), F (middle panels), and G (bottom panels). The histograms show the percentage of emission lines having radial velocities falling within each bin, with bin sizes $0.5\,km\,s^{-1}$ for the three clouds, corresponding to 1/3 of the mean intensity-weighted line width obtained for the dense gas tracers. The contribution from all CH_3OH transitions detected in each cloud has been considered. In each panel, the mean uncertainty for the central velocities of the single fittings is indicated. Black curves correspond to the Gaussian fitting obtained for $HN^{13}C$ in Section 4.1.1 (see also Fig. 3).

$$\chi(CH_3OH) = \frac{N_{tot}(CH_3OH)}{N_{tot}(H^{13}CO^+)} \frac{^{13}C}{^{12}C} \chi(HCO^+). \quad (6)$$

We assume a constant HCO^+ fractional abundance of $\sim 10^{-8}$ (Irvine, Goldsmith & Hjalmarson 1987) and a $^{12}C/^{13}C$ ratios of 40.2, 46.8, and 49.8 for clouds C, F, and G, respectively (Zeng et al. 2017). The $H^{13}CO^+$ column densities are calculated following the same method as that used for SiO (see above). In the selected positions, the narrow emission from SiO and CH_3OH and the $H^{13}CO^+$ emission show similar central velocities and line widths. χ(SiO) and $\chi(CH_3OH)$ of the narrow component range between 6.3×10^{-11}–7.4×10^{-10} and 0.9×10^{-8}–5.8×10^{-8} for cloud C, $\leq 3.8 \times 10^{-11}$–2.1×10^{-9} and 7.8×10^{-9}–6.4×10^{-8} for cloud F, and $\leq 3.2 \times 10^{-11}$–9.6×10^{-10} and 1.1×10^{-8}–5.5×10^{-8} for cloud G.

The CH_3OH and SiO emission detected towards the active cores F8, F9, C1, and C2 also shows broad line profiles. Hence, we evaluated the column densities of the SiO and CH_3OH broad components observed towards these positions. We assumed $T_{ex} = 50$ K, typical of shocked gas in molecular outflows (e.g. Jiménez-Serra et al. 2005), and we calculated the corresponding N_{tot} using MADCUBAIJ. Since no broad $H^{13}CO^+$ emission has been detected, we consider the 3σ upper limits to the $N_{tot}(H^{13}CO^+)$ to calculate the lower limits to

Downloaded from https://academic.oup.com/mnras/article/474/3/3760/4662631 by Biblioteca di Scienze tecnologiche user on 29 September 2020

Table 5. Column densities, ratios, and abundances of SiO, CH_3OH, and $H^{13}CO^+$ measured for the narrow and broad components in several positions towards the three clouds. NC = narrow component; BC = broad component.

		$N(H^{13}CO^+)$ ($\times10^{12}$ cm^{-2})		N(SiO) ($\times10^{12}$ cm^{-2})		$N(CH_3OH)$ ($\times10^{14}$ cm^{-2})		$\frac{N(SiO)}{N(H^{13}CO^+)}$		$\frac{N(CH_3OH)}{N(H^{13}CO^+)}$		χ(SiO) ($\times10^{-10}$)		$\chi(CH_3OH)$ ($\times10^{-8}$)	
	Position	NC	BC	NC	BC	NC	BC	NC	BC	NC	BC	NC	BC	NC	BC
C	C1	2.2	≤1.0–1.7	0.6	3.8	1.3	1.1	2.5	≥3.8	59.1	≥64.7	0.6	≥9.5	1.5	≥1.6
	C2	2.5	≤1.7	7.4	14	5.8	6.6	3.0	≥8.2	232.0	≥388.2	7.4	≥20.0	5.8	≥9.7
	C8	1.0	···	≤0.3	···	0.3	···	0.3	···	34.0	···	≤0.8	···	0.9	···
	(40, 90 arcsec)	0.8	···	0.4	···	0.6	···	0.5	···	72.5	···	1.2	···	1.8	···
F	F2	1.4	···	≤0.3	···	0.5	···	0.2	···	37.1	···	≤0.4	···	0.8	···
	F8	6.0	≤0.9–1.2	8.0	53.0	18.0	24.0	1.3	≥44.2	300.0	≥2696.6	2.8	≥92.8	6.3	≥56.6
	F9	3.3	≤1.3	3.3	54.0	10.0	7.7	1.0	≥41.5	303.0	≥592.3	2.1	≥87.2	6.4	≥12.4
	(−35, −20 arcsec)	0.6	···	6.4	···	1.6	···	10.2	···	254.0	···	21.0	···	5.3	···
G	G1	1.8	···	≤0.3	···	1.0	···	0.2	···	54.4	···	≤0.3	···	1.1	···
	G2	1.3	···	≤0.3	···	1.0	···	0.3	···	76.9	···	≤0.5	···	1.5	···
	G3	0.9	···	≤0.3	···	1.0	···	0.4	···	108.7	···	≤0.7	···	2.2	···
	(−28, 103 arcsec)	0.7	···	3.3	···	1.9	···	4.8	···	275.4	···	9.6	···	5.5	···

the abundance of SiO and CH_3OH using equations (5) and (6). The total column densities of the broad SiO and CH_3OH components are listed in Table 5 and correspond to χ(SiO) and $\chi(CH_3OH)$ in the range $\geq9.5\times10^{-10}$–2.0×10^{-9} and $\geq1.6\times10^{-8}$–9.7×10^{-8} for cloud C and $\geq8.7\times10^{-9}$–9.3×10^{-9} and $\geq1.2\times10^{-7}$–5.6×10^{-7} for cloud F. A similar analysis is not possible in cloud G since no broad component has been detected towards this cloud.

From Table 5, we find that the SiO/$H^{13}CO^+$ column density ratio for the narrow component is enhanced towards the active core positions in clouds C (e.g. C2) and F [e.g. F8, F9 and offset (−35, −20 arcsec)] by a factor of ≥5 with respect to the upper limits measured in cores C8 and F2. In cloud G, the narrow SiO emission is enhanced by more than a factor of 10 towards its peak position, with respect to the upper limits measured in the core positions G1, G2, and G3, which implies that the χ(SiO) towards the SiO peak in this cloud is enhanced by a factor of ∼10 with respect to the quiescent gas.

6 GAS MASS OF THE SUBSTRUCTURES

In this section, we provide rough estimates of the H_2 gas masses of all the velocity-coherent substructures identified in clouds C, F, and G from the emission of the dense gas tracers (see Section 4.1). To do this, we first calculate the total column density of $H^{13}CO^+$ within each velocity-coherent component by using its derived mean peak intensity $\langle I_{peak}\rangle$, its mean intensity-weighted line width $\langle\Delta v\rangle$, and the number of emission lines fitted for each substructure, n.

We assume an excitation temperature $T_{ex} = 9$ K for all components, as discussed in Section 5. The inferred values of $N(H^{13}CO^+)$ are converted into H_2 mass surface densities by using (see also Hernandez et al. 2012)

$$\Sigma_{H_2} = 2\mu_H \frac{^{12}C}{^{13}C} \frac{N(H^{13}CO^+)}{\chi(HCO^+)}, \quad (7)$$

where the mass per H nucleus is $\mu_H = 2.34\times10^{-24}$ gr, the assumed HCO^+ fractional abundance is $\chi(HCO^+) = 10^{-8}$ (Irvine et al. 1987) and the $^{12}C/^{13}C$ isotopic ratios for clouds C, F, and G are 40.2, 46.8, and 49.8, respectively (see Zeng et al. 2017). The H_2 gas mass of each velocity-coherent substructure is finally calculated by correcting by the pixel size area in units of cm^2. The obtained values are listed in Table 6.

From Table 6, it is clear that the main velocity component in all clouds (Fil2) is always more massive (by factors of ∼3–13) than their blue- (Fil1) and redshifted (Fil3) components. This is in agreement with previous studies towards other filamentary IRDCs, which employed low-density gas tracers such as ^{13}CO (Jiménez-Serra et al. 2014). As expected, the dense gas in each velocity component represents only a small fraction of the total mass of the cloud (as compared to the total gas masses derived from near- and mid-IR extinction mapping by Butler & Tan 2012 and Kainulainen & Tan 2013). A future study will establish the exact mass fractions of dense gas within these substructures by using large-scale maps of low-density gas tracers such as ^{13}CO and $C^{18}O$ obtained towards clouds C, F, and G.

7 DISCUSSION

In the past decade, several scenarios have been proposed to explain the formation of filamentary IRDCs. These include the flow-driven formation scenario and the cloud–cloud collision scenario. In the flow-driven scenario, rapid and warm atomic gas flows collide forming cold and filamentary structures due to thermal and gravitational instabilities (Vázquez-Semadeni, Ballesteros-Paredes & Klessen 2003; Van Loo et al. 2007; Hennebelle et al. 2008). The collision velocities are of tens of km s^{-1} and hence the emission of shock tracers (such as SiO and CH_3OH) is expected to be very broad and the separation in velocities between substructures within the clouds are expected to be important (Hennebelle et al. 2008). This first scenario presents major problems when a small magnetic field is considered (Körtgen & Banerjee 2015; Körtgen et al. 2016).

Alternatively, in the cloud–cloud collision scenario, already-molecular clouds collide at moderate velocities as a result of Galactic shear motions (which are ∼10 km s^{-1}; Li et al. 2017), and form

Downloaded from https://academic.oup.com/mnras/article/474/3/3760/4662631 by Biblioteca di Scienze tecnologiche user on 29 September 2020

Table 6. Mean peak intensity, mean intensity-weighted line width, number of fitted lines, $H^{13}CO^+$ total column density, H_2 gas mass surface densities, and gas masses derived for all velocity components identified in clouds C, F, and G.

		$\langle I_{peak} \rangle$ (K)	$\langle \Delta v \rangle$ (km s^{-1})	n	$N(H^{13}CO^+)$ ($\times 10^{13}$ cm^{-2})	Σ_{H_2} (gr cm^{-2})	M_{H_2} ($M_\odot$)
Cloud C	Fil1	0.24	1.47	58	2.0	0.4	227
	Fil2	0.29	2.05	155	8.8	1.7	988
	Fil3	0.21	1.06	30	6.6	0.1	74
Cloud F	Fil1	0.30	1.31	39	1.5	0.3	109
	Fil2	0.50	1.82	94	8.5	1.9	606
	Fil3	0.39	1.44	43	2.4	0.5	172
Cloud G	Fil1	0.25	1.59	30	1.2	0.3	55
	Fil2	0.30	1.87	74	4.1	1.0	192
	Fil3	0.22	1.45	44	1.4	0.3	65

filamentary structures that resemble IRDCs (Tan 2000; Tasker & Tan 2009; Van Loo et al. 2014; Wu et al. 2015, 2017a,b). In this second scenario, the gas is already molecular and therefore fossil records of the cloud–cloud collision, such as high-J CO line emission or emission from molecular shock tracers such as SiO or CH_3OH, are expected to be detected (Jiménez-Serra et al. 2010; Hernandez & Tan 2015; Pon et al. 2015, 2016a,b; Wu et al. 2015). Since the shock velocities involved are low ($\leq$10 km s^{-1}) the fossil record emission is expected to be narrow, as opposed to the flow-driven scenario, where the high velocities involved in the flow collision would produce broader shock tracer emission.

From our results in Section 4.1, it is clear that the kinematic and physical structure of IRDCs is complex and shows multiple velocity-coherent structures separated in velocity space by just a few km s^{-1} (ranging from 2.5 to 3.6 km s^{-1}; see Table 3), and which are clearly associated with the IRDC structures detected in extinction. This resembles the physical structure and kinematics of the molecular gas observed towards the filamentary IRDC G035.39−00.33 (already defined as cloud H; Henshaw et al. 2013; Jiménez-Serra et al. 2014). As with cloud H, the analysis of the emission of high-density gas tracers such as $H^{13}CO^+$ and $HN^{13}C$ suggests that these velocity-coherent structures are connected in velocity space towards the positions where massive dense cores are found in these clouds (see Fig. 4), which would support the cloud–cloud collision scenario.

In order to test this hypothesis, in Section 4.2 we have investigated the morphology and kinematics of the emission of two typical shock tracers, SiO and CH_3OH, to search for signatures of any possible cloud–cloud collision in clouds C, F, and G. SiO and CH_3OH indeed are widespread in the three clouds with spatial extents of a few parsecs across. In addition, the kinematics of these shock tracers show that clouds C and F present two clear line width components, i.e. a broad component showing line widths up to 30 km s^{-1} and a narrower component with line widths of $\leq$5 km s^{-1} (see Figs 8–10). In contrast, the SiO and CH_3OH emission from cloud G mainly shows narrow line profiles with a mean line width $<$2 km s^{-1}, i.e. even narrower than the emission found in clouds C and F. In the following, we discuss the possible origins of the two components observed in SiO and CH_3OH towards the three IRDCs analysed in our study.

7.1 SiO emission in clouds C and F

Cloud F has been extensively studied in previous works (Rathborne et al. 2005, 2008; Foster et al. 2014) and evidence for ongoing star formation activity has been found towards several regions in the cloud. Shepherd, Nürnberger & Bronfman (2004) and Rathborne et al. (2005, 2008) studied the massive active core F8 (see Rathborne et al. 2006; Butler & Tan 2009) and classified it as a hot molecular core powered by an embedded B0 protostar. Sanhueza et al. (2010) and Sakai et al. (2013) found a hot core/outflow system associated with core F9. Furthermore, Chambers et al. (2009) showed that most of the massive cores in the cloud have 24, 8, and 4.5 μm emission; and Foster et al. (2014), by performing deep near-IR images in *H* and *K* bands with the Keck telescopes, reported the presence of a distributed population of low-mass protostars in cloud F (see for instance, the embedded young cluster driving a collection of outflows coincident with the SiO emission peak detected at offset [−35, −20 arcsec]; see also Fig. 6).

From all this, it is not surprising that the broad SiO component contributes to almost 50 per cent of the total SiO emission measured in this cloud (see Table 4). The SiO line profiles are clearly broad towards the most active cores in cloud F (see e.g. cores F8 and F9 in Figs 6 and 7), and towards the positions with weaker SiO emission the SiO line profiles clearly show a blue- or redshifted broad component indicating that they are likely associated with outflow interaction (see offset [−35, −20 arcsec] in Fig. 7). This is supported by the fact that the abundances obtained for the SiO broad component are in agreement with those found in typical shocked outflowing gas (of some 10^{-9}–10^{-8}; see Martin-Pintado et al. 1992; Jiménez-Serra et al. 2005).

Signatures of ongoing star formation activity are also present in cloud C. Tan et al. (2016) and Kong et al. (2017) found a bipolar outflow in ^{12}CO (2–1) emission associated with core C1, while most of the other cores show emission at 24, 8, and 4.5 μm (Chambers et al. 2009). Feng et al. (2016) also reported a molecular outflow seen in SiO 2→1 emission towards core C1-S in this cloud, corresponding to a substructure in the C1 core of our sample. In fact, the SiO 2→1 line profiles measured towards this outflow show a combination of a narrow component centred at the velocity of the quiescent gas, and a broad component that appears red-/blueshifted by a few 10 km s^{-1} with respect to the ambient gas. As proposed by Feng et al. (2016), while the broad component is associated with the most evolved post-shocked gas (with abundances $> 10^{-9}$, similar to those reported in Section 5), the narrow SiO component would correspond to an early stage in the propagation of magnetohydrodynamic (MHD) shock waves characterized by the magnetic precursor (see also Jiménez-Serra et al. 2004, 2009). The abundance estimated by Feng et al. (2016) for this narrow component is $\sim 5 \times 10^{-12}$, i.e.

Downloaded from https://academic.oup.com/mnras/article/474/3/3760/4662631 by Biblioteca di Scienze tecnologiche user on 29 September 2020

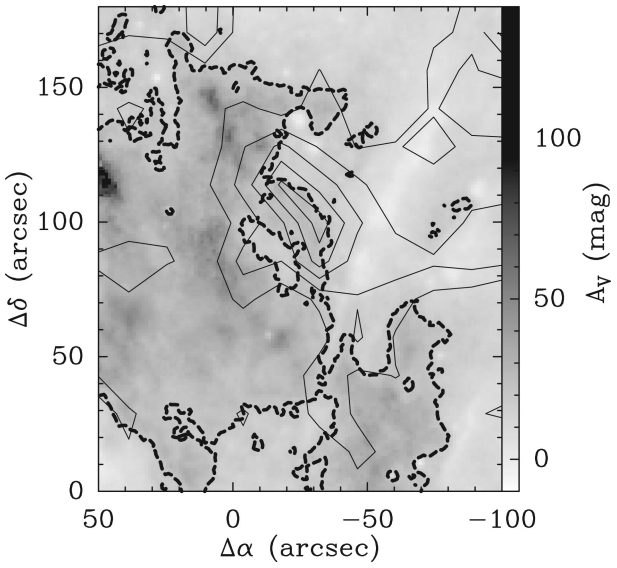

Figure 11. Integrated intensity map of the SiO line emission observed towards cloud G (solid contours) and superimposed on the A_V visual extinction map (grey-scale) derived by Kainulainen & Tan (2013). The velocity range for the SiO integrated intensity map is 35–50 km s^{-1} and the contour levels are 3σ, 6σ, 9σ, 12σ, and 15σ ($\sigma = 0.1$ K km s^{-1}). Dashed contour corresponds to a visual extinction of $A_V = 20$ mag.

~10 times lower than reported in Table 5 towards this core (C1). However, note that Feng et al. (2016) use interferometric data for the abundance estimation and it likely misses a significant fraction of the extended narrow SiO emission detected within the IRAM 30-m beam. It is therefore likely that the narrow and broad SiO emission detected in cloud C also arises from shocked gas in molecular outflows.

7.2 SiO emission in cloud G

As shown in Section 4.2, the SiO emission in cloud G only shows a narrow component having a mean line width of 1.6 km s^{-1}, whose emission peaks at a position off the IRDC [offset (−28, 103 arcsec)] and far away (56–167 arcsec, i.e. 0.8–2.3 pc) from the location of the massive cores detected in this cloud (see Fig. 6). In order to investigate the origin of this narrow SiO emission, we will investigate in detail this region of the cloud.

In Fig. 11, we compare the morphology of the SiO emission in cloud G with that of the A_V extinction map. With a dashed contour, we show the gas with dust extinctions higher than $A_V \sim 20$ mag. The comparison between the SiO emission and the dense gas in the cloud shows that SiO is extended and appears distributed mainly over the low extinction region in the map with $A_V \leq 20$ mag. However, the peak emission of SiO interestingly follows the spatial distribution of a dense ridge with $A_V \geq 20$ mag.

In Fig. 12, we compare the SiO emission distribution (white contours) with the 8 μm emission distribution (right-hand panel) and a three-colour image of the 3.6 μm (red), 4.5 μm (green), and 24 μm (blue) emission (left-hand panel), all obtained with the *Spitzer Space Telescope*. From Fig. 12, we find that most of the sources detected at 3.6 and 4.5 μm, and which overlap with the SiO emission, do not show any counterpart at 8 μm (only two 8 μm sources are detected towards the northern part of the SiO condensation). Emission at 4.5 μm is believed to be associated with shocked H_2 (Noriega-Crespo et al. 2004) or CO gas in outflows (Marston et al. 2004) and it is considered as an indirect evidence of on-going star formation if coupled with 8 μm emission (typically associated with deeply embedded protostars). In addition, the 3.6 and 4.5 μm sources are mainly located outside the $A_V = 20$ mag dense ridge and, therefore, it is unlikely that they represent young protostars driving outflows. Note that no 8 μm source is observed towards the location of the SiO/CH_3OH peak in cloud G.

Fig. 12 also shows much extended 4.5 μm emission running through the SiO extended emission from the north-west to the south-east (see magenta contours in both right- and left-hand panels). This emission is not associated with any 24 μm object (in blue in the left-hand panel) or 8 μm source in the region (grey-scale in right-hand panel), and it does not seem to have originated from any embedded protostar. Instead, it appears as an extended nebulosity containing a collection of 4.5 μm point sources. For this reason, and because the SiO emission does not peak towards this nebulosity (Fig. 12), it is unlikely that this extended 4.5 μm emission represents an outflow.

We speculate that the nebulous 4.5 μm emission is a remnant of a large-scale interaction. In this scenario, this interaction would have compressed the region towards the western edge of cloud G, yielding the $A_V = 20$ mag ridge seen in extinction. The extended SiO emission would then be a fossil record of this interaction. This idea would be supported by the fact that the radial velocities of SiO towards this condensation do not peak at the same velocity as the high-density gas probed by $HN^{13}C$, but appear at blueshifted velocities (see Fig. 9). Note that the histogram with the radial velocities of the narrow CH_3OH emission in cloud G also contains the contribution associated with the bulk of the IRDC and, as a result, it does not show the same pattern as the narrow SiO. The spread in velocities observed for SiO would support the cloud–cloud collision scenario, since it is expected from simulations of cloud–cloud collisions (Wu et al. 2017a,b). In addition, the differences in the kinematics of the SiO emission and the high-density gas may indicate that the gas compressed in the large-scale interaction did not have enough time to relax to the velocities of the bulk of the gas in the IRDC. This interaction had to be relatively gentle since the SiO emission shows line widths $\leq$3 km s^{-1} (see Fig. 8), which are much narrower than the ones found in clouds C and F.

Alternatively, the compression of the molecular gas in the $A_V = 20$ mag dense ridge may have triggered the formation of a population of low-mass protostars. Bipolar outflows driven by the newly formed low-mass stars could be responsible for the presence of the detected SiO emission (Martin-Pintado, Bachiller & Fuente 1992; Zhang, Ho & Wright 2000). In this scenario, the axis of the putative outflows would have to be close to the plane of the sky, with their redshifted lobes being screened by the $A_V = 20$ mag dense ridge. This configuration would explain the narrow SiO line profiles in cloud G that peak mostly at blueshifted velocities. As recently shown by Stephens et al. (2017), such a configuration is highly unlikely since molecular outflows are found to be randomly oriented with respect to the molecular filaments in which they are embedded. In addition, projection effects are not expected to play a major role in the line width distribution of SiO in IRDCs, since the probability to detect outflows with broad emission assuming a random distribution of outflow inclination angles, is significantly lower than that to detect outflows with narrow SiO lines (see section 3.2 in Beuther & Sridharan 2007). This is in contradiction with observations.

Narrow SiO emission has also been detected in very young outflows and proposed to be driven by the early stages of the propagation of MHD shock waves (i.e. via the magnetic precursor; see Jiménez-Serra et al. 2004, 2005). This kind of emission is however

Downloaded from https://academic.oup.com/mnras/article/474/3/3760/4662631 by Biblioteca di Scienze tecnologiche user on 29 September 2020

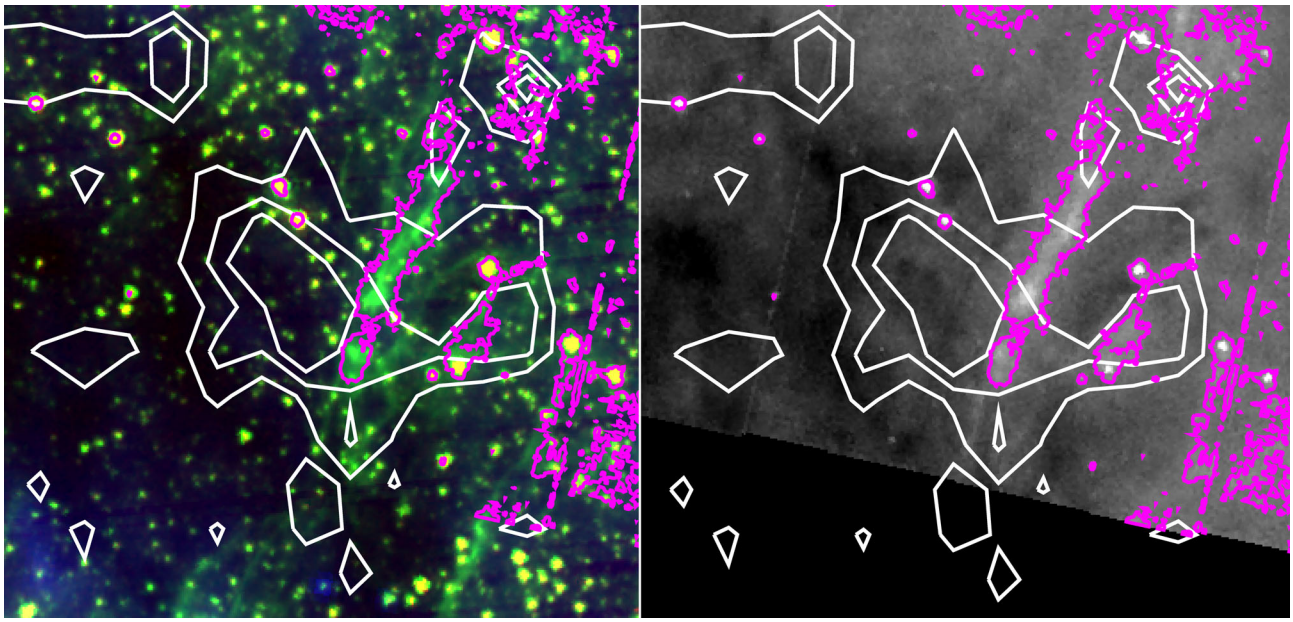

Figure 12. Comparison of the SiO emission (white contours) with emissions at 3.6, 4.5, 8, and 24 μm, towards cloud G as obtained with the *Spitzer Space Telescope*. Left-hand panel: *Spitzer* three-colour image with 3.6 μm emission displayed in red, 4.5 μm emission in green, and 24 μm emission in blue. Right-hand panel: 8 μm emission towards cloud G displayed in grey-scale. In both panels the SiO emission levels (white contours) correspond to 3σ, 6σ, and 9σ, with $\sigma = 0.1\,\mathrm{K\,km\,s^{-1}}$. The 4.5 μm nebulosity is highlighted by the magenta contour corresponding to the 12σ level at 4.5 μm and 100σ level at 8 μm.

rare and it has only been reported towards two sources (Jiménez-Serra et al. 2004; Feng et al. 2016). Another possibility would be that narrow SiO originates from shocked gas that has been decelerated by the interaction with the surrounding molecular gas envelope (see Lefloch et al. 1998). In this scenario, the extension of narrow SiO emission detected in cloud G would require ∼70 outflow sources for which their associated shocked gas would have been decelerated by the interaction with the $A_v = 20$ mag extinction ridge. Higher angular resolution observations are therefore needed to establish the origin of narrow SiO in cloud G.

Finally, we note that it is very unlikely that the SiO emission detected in cloud G is arising from the merging of the internal substructures found in the dense gas (see Section 4.1.1), due to the fact that the separation in velocities is too low to account for the observed abundance towards the SiO peak. This is also supported by the fact that the substructures detected in cloud G do not spatially overlap in the region where the SiO emission is present.

7.3 SiO in actively star-forming ridges: comparison with previous works

The emission from the 2→1 rotational transition of SiO has also been studied towards at least two very active high-mass star-forming regions: W43 (Motte, Schilke & Lis 2003; Nguyen-Luong et al. 2011, 2013; Louvet et al. 2014, 2016) and Cygnus X (Wendker, Higgs & Landecker 1991; Schneider et al. 2006; Motte et al. 2007; Duarte-Cabral et al. 2014; Duarte-Cabral & Dobbs 2016). These regions are both classified as ministarburts due to their high level of star formation activity, and their extended emission of SiO has been proposed to have originated in large-scale interactions (Nguyen-Luong et al. 2013; Louvet et al. 2016). The SiO lines detected towards W43 show a single Gaussian line profile with typical line widths $\geq 6\,\mathrm{km\,s^{-1}}$ (Nguyen-Luong et al. 2013; Louvet et al. 2016) and a mean SiO total column density of $6 \times 10^{13}\,\mathrm{cm^{-2}}$ has been estimated for this source (see Nguyen-Luong et al. 2013; Louvet et al. 2016). A similar analysis has been performed on Cygnus X by Motte et al. (2007) and Duarte-Cabral et al. (2014). The authors identified two line width components in the SiO line profiles: a very broad emission with line widths $\sim 17\,\mathrm{km\,s^{-1}}$ and a narrower emission with line widths in the range of 3–6 $\mathrm{km\,s^{-1}}$. Duarte-Cabral et al. (2014) report a SiO total column density of $0.1\text{–}4 \times 10^{12}\,\mathrm{cm^{-2}}$ towards Cygnus X.

If we compare the properties of the SiO emission towards W43 and Cygnus X with our results from cloud G, we find that the SiO emission detected in W43 shows broader line profiles than those from cloud G ($\geq 6\,\mathrm{km\,s^{-1}}$ in W43 versus $\leq 3\,\mathrm{km\,s^{-1}}$ in cloud G; see Fig. 8), and the total column density in W43 is higher by a factor of ≥20 with respect to that found in cloud G. On the other hand, the SiO line width and the total column density estimated towards Cygnus X are comparable with the results found in cloud G and presented in Table 5. However, both W43 and Cygnus X show a level of star formation activity that is much higher than that of cloud G. This suggests that W43 and Cygnus X are in a more evolved evolutionary stage than cloud G and, therefore, the SiO extended emission detected towards these sources may be affected/influenced by star formation. Cloud G may thus represent a unique case where the effects of large-scale interactions can be tested *before the onset of star formation.*

The SiO emission detected in W43 and Cygnus X is comparable to our results from clouds C and F. Both the broad and narrow SiO components detected in the two clouds show line widths similar to that in W43 and Cygnus X and the SiO total column density in W43 is comparable to those listed in Table 5 for the two clouds of our sample. This similarity and the fact that all the four sources are hosting active sites of star formation would be an evidence of the common star formation related origin of the SiO emission towards such sources.

Downloaded from https://academic.oup.com/mnras/article/474/3/3760/4662631 by Biblioteca di Scienze tecnologiche user on 29 September 2020

7.4 CH_3OH emission in IRDCs

As with the SiO emission, the CH_3OH line profile shows a very broad line width component towards clouds C and F, the most active clouds of the sample. This broad component shows properties very similar to those of the broad SiO emission in the two clouds, i.e. they show a similar spatial distribution and mean line width. It is hence likely that, as for SiO, the CH_3OH broad emission arises from post-shocked gas in molecular outflows (see Jiménez-Serra et al. 2005; Tafalla et al. 2010). This is supported by the fact that the CH_3OH broad component represents less than 0.1 per cent of the total emission in cloud G, where the star formation activity is much lower.

As discussed in Section 4.2, the CH_3OH emission also shows a very narrow line width component in all the three clouds. This narrow component is very extended in all of the three clouds and, in particular, in cloud G where it is found to only be narrow (see Section 4.2). From the bottom panels of Fig. 6, both SiO and CH_3OH emission are enhanced towards the north-west region of cloud G and hence it is likely that towards this region the two molecules are affected by the same physical process and thus have the same origin (either large-scale interaction or a young population of low-mass protostars; see Section 7.2). The abundance of narrow CH_3OH derived towards this position is indeed a factor of $\geq$2 higher than towards the quiescent cores G1, G2, and G3. However, unlike SiO, CH_3OH shows narrow emission associated with the bulk of the IRDC, where no SiO is detected. Narrow CH_3OH towards the cores in cloud G cannot be due to star formation because these cores are quiescent and do not show any signature of on-going star formation (see Chambers et al. 2009). Hence, some additional mechanism has to be responsible for this emission. This is also true for clouds C and F, where narrow CH_3OH appears more extended than the narrow SiO component. The narrow emission of CH_3OH also peaks at the radial velocity of the clouds (see Fig. 10), indicating that most of this emission is related to the quiescent gas.

Several mechanisms can account for the release of CH_3OH into the gas phase. These include UV-induced photodesorption and chemical reactive desorption.[4] As reported by Martín-Doménech, Muñoz Caro & Cruz-Díaz (2016), UV-induced photodesorption is very unlikely since UV photons dissociate CH_3OH into radicals forming smaller molecules such as CO, CO_2, and H_2CO that are then released into the gas phase. On the other hand, chemical reactive desorption allows the desorption of CH_3OH itself after its formation on grain surfaces via hydrogenation, representing a viable mechanism for the production of narrow CH_3OH in IRDCs not associated with star formation. This process also explains the presence of CH_3OH and other complex organics in the gas phase of pre-stellar cores such as L1498, L1517B, and L1544 (Bizzocchi et al. 2014; Jiménez-Serra et al. 2016; Vasyunin et al. 2017). The abundance of CH_3OH in the L1544 pre-stellar core is $\sim 6 \times 10^{-9}$ (Vastel et al. 2014), which is comparable to the CH_3OH abundances estimated towards clouds C, F, and G in the quiescent gas for the narrow component (see Table 5).

The presence of internal shocks of a few km s^{-1} can also be responsible for the narrow CH_3OH emission in IRDCs (Pon et al. 2015). These shocks are due to virialized motions of the gas within the clouds and could possibly account for the estimated CH_3OH abundance. However, at the current spatial resolution it is not possible to resolve such internal shocks. We exclude the scenario of thermal desorption in the quiescent regions of clouds C, F, and G because the typical temperatures of IRDCs ($\leq$20 K; Pillai et al. 2006) are much lower than that required for CH_3OH to evaporate (Collings et al. 2004). However, note that this desorption mechanism is possibly responsible for the narrow CH_3OH lines detected towards star-forming cores in clouds C and F because they likely arise from the hot envelopes around young protostars.

[4] In the process of chemical reactive desorption, the newly formed molecule possesses an energy surplus that allows it to evaporate (see Minissale et al. 2016).

8 CONCLUSIONS

Using the IRAM 30-m single-dish telescope, we performed a detailed analysis of the $H^{13}CO^+$, $HN^{13}C$, SiO, and CH_3OH emission towards three filamentary IRDCs: G028.37+00.07, G034.43+00.24, and G034.77−00.55 (clouds C, F, and G, respectively). We investigated the spatial distribution and kinematics of dense gas ($H^{13}CO^+$ and $HN^{13}C$) and shock (SiO and CH_3OH) tracers. We studied the line profiles for all the transitions, including studying the line width and central velocity distributions. The results we obtained can be summarized as follows.

(i) In all three clouds of our sample, the dense gas emission shows multiple velocity components corresponding to three independent substructures that are spatially and kinematically well defined. The brightest substructures probe the ambient gas moving at the central velocity of the clouds, while the red- and blueshifted substructures have velocity drifts of $\sim$1 km s^{-1} with respect to the central velocity of the clouds.

(ii) The $H^{13}CO^+$ and $HN^{13}C$ emission lines show similar line width, always $\leq$5 km s^{-1}. The mean line width values (in the range 1.8–1.6 km s^{-1}) obtained for the two molecules are comparable in the three clouds. Furthermore, from the line width distributions shown in Fig. 5 only one line width component can be identified.

(iii) The spatial distribution of shock tracers is widespread at a parsec-scale in all the clouds. In clouds C and F the emission is also affected by the presence of several active cores, while in cloud G, the SiO and CH_3OH emission distributions are very different. In this cloud the SiO emission is concentrated around its peak, in the north-east region, while the CH_3OH emission is distributed along the cloud and follows well its filamentary structure. In both cases, the emission distribution is not correlated with the (inactive) cores of the cloud.

(iv) The shock tracers' emission shows multiple line width components: a narrow ($\leq$5 km s^{-1}), widespread component across the clouds that is present in almost every position with significant emission, and a broad (up to 30 km s^{-1}) component that is strictly related to the positions of the cores in the cloud. In clouds C and F, both components are detected. In cloud G, the SiO emission is only narrow, while for the CH_3OH emission, 0.1 per cent of the total emission present lines broader than 5 km s^{-1}. However, this small fraction presents line width always <6 km s^{-1} and is not significant compared to the total emission.

(v) Neither the broad nor the narrow component in the SiO and CH_3OH emission follows the high-density subfilamentary structure. Furthermore, the broad component is distributed along a wide velocity range, while the narrow component is less extended in velocity. Narrow SiO emission in cloud G shows a radial velocity distribution skewed to blueshifted velocities.

(vi) In clouds C and F, the shock tracers' emission is likely due to the ongoing star formation activity. The presence of outflows in these clouds would be responsible for both the broad and the narrow

Downloaded from https://academic.oup.com/mnras/article/474/3/3760/4662631 by Biblioteca di Scienze tecnologiche user on 29 September 2020

components, corresponding to the post-shocked gas and the early stage in the propagation of MHD shock waves, respectively.

(vii) In cloud G, the very low level of star formation activity and the very narrow line width of the shock tracers' emission suggest a different origin for the SiO and the enhanced CH_3OH emission towards the north-west of this cloud. Particularly, the SiO emission could be a fossil record of a previous large-scale interaction occurring nearby. As a second possibility, the mentioned large-scale interaction could have triggered the formation of a low-mass star population within a $A_v = 20$ mag extinction ridge, whose SiO emission originates from outflows. Such outflows should show an almost parallel orientation in the plane of the sky with their redshifted lobes being screened by the $A_v = 20$ mag ridge.

(viii) The narrow CH_3OH emission in cloud G is more extended than the corresponding SiO emission and shows velocities very close to the central velocity of the cloud. Hence, it is mainly associated with the quiescent gas and it is likely produced by the chemical-reactive desorption mechanism.

ACKNOWLEDGEMENTS

This paper is based on observations carried out with the IRAM 30-m telescope under projects 134-12 and 027-13. IRAM is supported by INSU/CNRS (France), MPG (Germany), and IGN (Spain). We thank the anonymous referee for their comments that have helped to improve the clarity of this paper. IJ-S acknowledges the financial support received from the People Programme (Marie Curie Actions) of the European Union's Seventh Framework Programme (FP7/2007-2013) under REA grant agreement PIIF-GA-2011-301538, and from the STFC through an Ernest Rutherford Fellowship (proposal number ST/L004801). The research leading to these results has also received funding from the European Commission (FP/2007-2013) under grant agreement No 283393 (RadioNet3). PC acknowledges support from the European Research Council (ERC; project PALs 320620). Partial salary support for AP was provided by a Canadian Institute for Theoretical Astrophysics (CITA) National Fellowship.

REFERENCES

Akaike H., 1974, IEEE Trans. Automatic Control, 19, 716
Bachiller R., Pérez Gutiérrez M., Kumar M. S. N., Tafalla M., 2001, A&A, 372, 899
Beuther H., Sridharan T. K., 2007, ApJ, 668, 348
Bizzocchi L., Caselli P., Spezzano S., Leonardo E., 2014, A&A, 569, A27
Butler M. J., Tan J. C., 2009, ApJ, 696, 484
Butler M. J., Tan J. C., 2012, ApJ, 754, 5
Chambers E. T., Jackson J. M., Rathborne J. M., Simon R., 2009, ApJS, 181, 360
Collings M. P., Anderson M. A., Chen R., Dever J. W., Viti S., Williams D. A., McCoustra M. R. S., 2004, MNRAS, 354, 1133
Csengeri T. et al., 2016, A&A, 586, A149
Duarte-Cabral A., Dobbs C. L., 2016, MNRAS, 458, 3667
Duarte-Cabral A., Bontemps S., Motte F., Gusdorf A., Csengeri T., Schneider N., Louvet F., 2014, A&A, 570, A1
Egan M. P., Shipman R. F., Price S. D., Carey S. J., Clark F. O., Cohen M., 1998, ApJ, 494, L199
Feng S., Beuther H., Zhang Q., Liu H. B., Zhang Z., Wang K., Qiu K., 2016, ApJ, 828, 100
Foster J. B. et al., 2014, ApJ, 791, 108
Heitsch F., Ballesteros-Paredes J., Hartmann L., 2009, ApJ, 704, 1735
Hennebelle P., Banerjee R., Vázquez-Semadeni E., Klessen R. S., Audit E., 2008, A&A, 486, L43
Henshaw J. D., Caselli P., Fontani F., Jiménez-Serra I., Tan J. C., Hernandez A. K., 2013, MNRAS, 428, 3425
Henshaw J. D., Caselli P., Fontani F., Jiménez-Serra I., Tan J. C., 2014, MNRAS, 440, 2860
Henshaw J. D. et al., 2016, MNRAS, 457, 2675
Hernandez A. K., Tan J. C., 2015, ApJ, 809, 154
Hezareh T., Houde M., McCoey C., Li H.-b., 2010, ApJ, 720, 603
Irvine W. M., Goldsmith P. F., Hjalmarson A., 1987, in Hollenbach D. J., Thronson H. A. Jr, eds, Astrophysics and Space Science Library, Vol. 134, Interstellar Processes. Reidel, Dordrecht, p. 561
Jiménez-Serra I., Martín-Pintado J., Rodríguez-Franco A., Marcelino N., 2004, ApJ, 603, L49
Jiménez-Serra I., Martín-Pintado J., Rodríguez-Franco A., Martín S., 2005, ApJ, 627, L121
Jiménez-Serra I., Caselli P., Martín-Pintado J., Hartquist T. W., 2008, A&A, 482, 549
Jiménez-Serra I., Martín-Pintado J., Caselli P., Viti S., Rodríguez-Franco A., 2009, ApJ, 695, 149
Jiménez-Serra I., Caselli P., Tan J. C., Hernandez A. K., Fontani F., Butler M. J., van Loo S., 2010, MNRAS, 406, 187
Jiménez-Serra I., Caselli P., Fontani F., Tan J. C., Henshaw J. D., Kainulainen J., Hernandez A. K., 2014, MNRAS, 439, 1996
Jiménez-Serra I. et al., 2016, ApJ, 830, L6
Kainulainen J., Tan J. C., 2013, A&A, 549, A53
Kong S., Tan J. C., Caselli P., Fontani F., Wang K., Butler M. J., 2017, preprint (arXiv:1701.05953)
Körtgen B., Banerjee R., 2015, MNRAS, 451, 3340
Körtgen B., Seifried D., Banerjee R., Vázquez-Semadeni E., Zamora-Avilés M., 2016, MNRAS, 459, 3460
Lefloch B., Castets A., Cernicharo J., Loinard L., 1998, ApJ, 504, L109
Li Q., Tan J. C., Christie D., Bisbas T. G., Wu B., 2017, PASJ, (arXiv:1706.03764)
Louvet F. et al., 2014, A&A, 570, A15
Louvet F. et al., 2016, A&A, 595, A122
Marston A. P. et al., 2004, ApJS, 154, 333
Martín-Doménech R., Muñoz Caro G. M., Cruz-Díaz G. A., 2016, A&A, 589, A107
Martin-Pintado J., Bachiller R., Fuente A., 1992, A&A, 254, 315
Minissale M., Dulieu F., Cazaux S., Hocuk S., 2016, A&A, 585, A24
Motte F., Schilke P., Lis D. C., 2003, ApJ, 582, 277
Motte F., Bontemps S., Schilke P., Schneider N., Menten K. M., Broguière D., 2007, A&A, 476, 1243
Müller H. S. P., Schlöder F., Stutzki J., Schlemmer S., Giesen T., Schilke P., 2005, IAU Symp. 235, Astrochemistry: Recent Successes and Current. p. 62
Nguyen-Luong Q. et al., 2011, A&A, 529, A41
Nguyen-Luong Q. et al., 2013, ApJ, 775, 88
Noriega-Crespo A., Carey S., Eisloffel J., Latter W., Marleau F., Morris P., Raga A., Stapelfeldt K., 2004, Emission from H2, PAHs, and Warm Dust in Proto-stellar Jets. Spitzer Proposal ID 3315
Perault M. et al., 1996, A&A, 315, L165
Peretto N., Fuller G. A., 2010, ApJ, 723, 555
Pillai T., Wyrowski F., Menten K. M., Krügel E., 2006, A&A, 447, 929
Pon A., Caselli P., Johnstone D., Kaufman M., Butler M. J., Fontani F., Jiménez-Serra I., Tan J. C., 2015, A&A, 577, A75
Pon A. et al., 2016a, A&A, 587, A96
Pon A. et al., 2016b, ApJ, 827, 107
Rathborne J. M., Jackson J. M., Chambers E. T., Simon R., Shipman R., Frieswijk W., 2005, ApJ, 630, L181
Rathborne J. M., Jackson J. M., Simon R., 2006, ApJ, 641, 389
Rathborne J. M., Jackson J. M., Zhang Q., Simon R., 2008, ApJ, 689, 1141
Rathborne J. M., Jackson J. M., Simon R., Zhang Q., 2009, Ap&SS, 324, 155
Rathborne J. M., Garay G., Jackson J. M., Longmore S., Zhang Q., Simon R., 2011, ApJ, 741, 120
Rivilla V. M., Fontani F., Beltrán M. T., Vasyunin A., Caselli P., Martín-Pintado J., Cesaroni R., 2016, ApJ, 826, 161

Downloaded from https://academic.oup.com/mnras/article/474/3/3760/4662631 by Biblioteca di Scienze tecnologiche user on 29 September 2020

Sakai T. et al., 2013, ApJ, 775, L31
Sanhueza P., Garay G., Bronfman L., Mardones D., May J., Saito M., 2010, ApJ, 715, 18
Schilke P., Walmsley C. M., Pineau des Forets G., Flower D. R., 1997, A&A, 321, 293
Schneider N., Bontemps S., Simon R., Jakob H., Motte F., Miller M., Kramer C., Stutzki J., 2006, A&A, 458, 855
Shepherd D. S., Nürnberger D. E. A., Bronfman L., 2004, ApJ, 602, 850
Simon R., Rathborne J. M., Shah R. Y., Jackson J. M., Chambers E. T., 2006, ApJ, 653, 1325
Stephens I. W. et al., 2017, ApJ, 846, 16
Tafalla M., Santiago-García J., Hacar A., Bachiller R., 2010, A&A, 522, A91
Tan J. C., 2000, ApJ, 536, 173
Tan J. C., Kong S., Zhang Y., Fontani F., Caselli P., Butler M. J., 2016, ApJ, 821, L3
Tasker E. J., Tan J. C., 2009, ApJ, 700, 358
Van Loo S., Falle S. A. E. G., Hartquist T. W., Moore T. J. T., 2007, A&A, 471, 213
Van Loo S., Keto E., Zhang Q., 2014, ApJ, 789, 37
Vastel C., Ceccarelli C., Lefloch B., Bachiller R., 2014, ApJ, 795, L2
Vasyunin A. I., Caselli P., Dulieu F., Jiménez-Serra I., 2017, ApJ, 842, 33
Vázquez-Semadeni E., Ballesteros-Paredes J., Klessen R., 2003, in De Buizer J. M., van der Bliek N. S., eds, ASP Conf. Ser. Vol. 287, Galactic Star Formation Across the Stellar Mass Spectrum. Astron. Soc. Pac., San Francisco, p. 81
Wang K., Zhang Q., Wu Y., Zhang H., 2011, ApJ, 735, 64
Wendker H. J., Higgs L. A., Landecker T. L., 1991, A&A, 241, 551
Wu B., Van Loo S., Tan J. C., Bruderer S., 2015, ApJ, 811, 56
Wu B., Tan J. C., Van Loo S., Nakamura F., Bruderer S., 2016, Am. Astron. Soc. Meeting Abstr., 227, 319.02
Wu B., Tan J. C., Nakamura F., Van Loo S., Christie D., Collins D., 2017a, ApJ, 835, 137
Wu B., Tan J. C., Christie D., Nakamura F., Van Loo S., Collins D., 2017b, ApJ, 841, 88
Zeng S. et al., 2017, A&A, 603, A22
Zhang Q., Ho P. T. P., Wright M. C. H., 2000, AJ, 119, 1345
Zhang Q. et al., 2014, ApJ, 792, 116

This paper has been typeset from a TEX/LATEX file prepared by the author.

Downloaded from https://academic.oup.com/mnras/article/474/3/3760/4662631 by Biblioteca di Scienze tecnologiche user on 29 September 2020